Chemico-Biological Interactions 430 (2026) 111971

Contents lists available at ScienceDirect

Chemico-Biological Interactions

journal homepage: www.elsevier.com/locate/chembioint

Research paper

Targeting the lipid membrane to prevent viral entry: the case of a C18-alkylated EGCG compound

Cristina Minnelli [a,1], Sara Caucci [b,1], Roberta Galeazzi [a], Emiliano Laudadio [c], Elena Romagnoli [a], Andrea Frontini [a], Loredana Rao [a], Valentina Notarstefano [d], Tatiana Armeni [e], Brenda Romaldi [e], Stefano Menzo [b,*], Giovanna Mobbili [a,**]

[a] Department of Life and Environmental Sciences, Polytechnic University of Marche, 60131, Ancona, Italy
[b] Department of Biomedical Sciences and Public Health, Polytechnic University of Marche, Ancona, Italy
[c] Department of Science and Engineering of Matter, Environment and Urban Planning, Polytechnic University of Marche, 60131, Ancona, Italy
[d] Department of Bioscience and Technology for Agriculture, Food and Environment, University of Teramo, 64100, Teramo, Italy
[e] Department of Specialist Clinical Sciences and Odontostomatology, School of Medicine, Marche Polytechnic University, 60131, Ancona, Italy

A B S T R A C T

Viruses depend on host cell membrane trafficking machinery for most stages of their life cycle, including viral entry, assembly, and immune evasion. Accordingly, alteration in membrane lipid composition and organization may impair viral access to host cells. In this work, we synthesized a series of lipophilic derivatives of Epigallocatechin-3-gallate (EGCG) and evaluated their SARS-CoV-2 inhibitory activity in an *in vitro* model. Among them, EGCG-C18, a 4″-octadecyl EGCG derivative obtained by regio-selective alkylation of the natural polyphenol resulted as the most promising drug candidate. The localization of EGCG-C18 within the cell membrane was assessed by Fourier Transform InfraRed and Raman Microspectroscopy (FTIRM and RMS), while its interaction with monosialotetrahexosylganglioside (GM1), a glycosphingolipid present in specific microdomains of the plasma membrane, known as lipid rafts, was investigated using Molecular Dynamics (MD) simulation, flow cytometry, and confocal microscopy. EGCG-C18 seems to prevent viruses from entering cells by directly impacting the organization of GM1. In addition, we demonstrated that EGCG-C18 treatment decreases EGFR activation, introducing other potential actions of this compound. Finally, EGCG-C18 was evaluated against Herpes Simplex, Influenza B, and HIV-1, to test the hypothesis of a broad-spectrum antiviral activity, potentially driven by its ability to reorganize lipid raft components.

1. Introduction

Membrane-targeted therapies against SARS-CoV-2 represent a promising alternative to conventional antiviral strategies by modulating the physicochemical properties of the host cell plasma membrane and thereby interfering with virus–cell interactions and entry processes [1]. The initial contact between many viruses and host cells occurs at the level of the plasma membrane, where membrane organization and lipid composition critically influence receptor accessibility and viral attachment. In this context, cholesterol- and sphingolipid-enriched membrane microdomains, commonly referred to as lipid rafts (LRs), contribute to the lateral organization of the membrane and can act as dynamic platforms facilitating viral binding and internalization [2–4]. LRs are thought to promote the clustering of viral receptors and co-receptors, thereby enhancing infection efficiency for both enveloped and non-enveloped viruses. For instance, the engagement of angiotensin-converting enzyme 2 (ACE2) by the spike (S) glycoprotein is the early step in the entry process of SARS-CoV and SARS-CoV-2 into the host cells [5,6]. Similarly, HIV-1 entry [7] involves the interaction of viral gp120 with CD4 and the co-receptors CCR5 and CXCR4, whose signalling and membrane organization are regulated by cholesterol-rich domains [8–10]. Human herpes virus-6 (HHV-6) has also been reported to exploit membrane microdomain reorganization during cell entry by recruiting its cellular receptor CD46 into raft-enriched regions [11–14]. Multiple experimental and computational studies further indicate that viral entry frequently involves recognition of specific gangliosides, such as GM1, enriched in lipid rafts, with GM1–virus interactions thought to facilitate subsequent receptor engagement and internalization, thereby contributing to efficient infection [7,15–18]. Consistent with this concept, agents capable of inducing lipid raft or GM1 perturbations

* Corresponding author.
** Corresponding author.
E-mail addresses: s.menzo@univpm.it (S. Menzo), g.mobbili@univpm.it (G. Mobbili).
[1] contribute equally.

https://doi.org/10.1016/j.cbi.2026.111971
Received 6 November 2025; Received in revised form 31 January 2026; Accepted 12 February 2026
Available online 14 February 2026

[19], are expected to interfere with the sites of initial binding, activation, internalization, and cell-to-cell transmission of enveloped viruses including Sars-CoV-2 [20–22]; for example, agents such as methyl--β-cyclodextrins can have an anti-viral role [23] thank to their peculiar shape capable of sequestering cholesterol by forming an inclusion complex. It has been shown that cholesterol depletion in Vero E6 (African green monkey kidney) cells reduced pseudo-typed SARS-CoV infectivity by 90% by replacing ACE2 in a non-raft environment [24].

Amphiphilic compounds are particularly well suited to modulate membrane organization, as they can insert into lipid bilayers through interactions with both hydrophobic and hydrophilic environments [25]. By altering lipid packing and membrane order, such compounds may indirectly affect the size, stability, and functional properties of lipid rafts, ultimately impairing signaling pathways and protein localization associated with these domains [26]. In this context, epigallocatechin-3-gallate (EGCG), the most abundant polyphenol in green tea, has attracted considerable interest due to its reported antiviral activity against a range of viruses, including coronaviruses. While it primarily works by binding to the spike proteins on the virus surface, thereby preventing the virus from attaching to and entering host cells [27], evidence also suggests a preventive effect that may be partly related to its interaction with membrane lipids. EGCG has been shown to associate with the cell surface in a heterogeneous manner, with preferential partitioning into raft-enriched membrane fractions [28]. Incorporation of EGCG into cellular membranes can alter lipid order, potentially destabilising lipid raft-dependent processes involved in viral internalization [29]. Based on these observations, we synthesized a series of lipophilic EGCG derivatives to enhance the ability of the parent compound to interact with the membrane lipid bilayer. To further investigate the structural requirements relevant to the potential membrane-targeting antiviral, we also prepared an Edaravone-C18 and an Epicatechin-C18. The antiviral activity of the synthesized compounds was evaluated in Vero E6 cells, identifying EGCG-C18 as the most effective molecule. Incorporation of EGCG-C18 into the plasma membrane was demonstrated by Fourier-transform infrared and Raman microspectroscopy (FTIR and RMS), supporting its ability to directly interact with the lipid bilayer.

Given that membrane organization critically regulates the activity of membrane-associated receptors, the effect of EGCG-C18 on epidermal growth factor receptor (EGFR) expression and activation was investigated as a functional readout of membrane perturbation. In parallel, the impact of EGCG-C18 on GM1, a glycosphingolipid enriched in lipid raft microdomains, was examined using molecular dynamics simulations, flow cytometry, and confocal microscopy, serving as an indicator of alterations in raft-associated lipid domains potentially involved in viral entry processes. Finally, based on the hypothesis that membrane-targeting drugs can act against different viral infections (unlike those against virus-specific targets) by destabilising common processes of viral infection, such as membrane fusion and cell entry, we tested EGCG-C18 against Herpes Simplex virus, Influenza B, and HIV-1.

2. Results and discussion

2.1. Rationale of the drug choice and synthesis

Previous studies [27,30] have shown that the anti-SARS-CoV-2 activity of EGCG is primarily attributed to its ability to bind to the receptor-binding domain (RBD) of the viral spike (S) protein, thereby preventing the virus from interacting with the ACE2 receptor on host cells. However, a weak antiviral effect has been observed that may partly result from interactions of the polyphenol with the cellular membrane upstream of RBD binding [31]; the experimental evidence shows that in the interaction with cell membranes, EGCG tends to associate particularly with LR domains [28], suggesting a potential role in the modulation of their organisation and fluidity [32]. Since lipids with long and saturated alkyl chains preferentially partition into the LR-ordered domains [33], in this study, we employed a series of 4″-alkyl EGCG lipophilic derivatives obtained by regio-selective alkylation of the natural polyphenol at the 4″ hydroxyl group in the D-ring (Scheme 1) and previously synthesized by our group and by others to be used as lipophilic antioxidants or antitumoral [34,35].

To investigate how the length of the alkyl chain could affect antiviral activity, we chose three 4″-alkyl EGCG characterised by the presence of linear saturated alkyl chains containing 6, 10, and 18 carbon atoms connected to the epigallocatechin nucleus with an ethereal bond at position 4". We also synthesized an Epicatechin-C18 (EC-C18) using a synthetic route similar to that described for the 4″-alkyl EGCG derivatives along with an Edaravone-C18 (EdV-C18), featuring an 18-atom C chain (Fig. 1) and already known as a lipophilic antioxidant [36]. Both compounds were chosen to understand the influence of the drug's hydrophilic portion in contrasting virus entry: EdV-C18 for its lack of hydroxyl groups, and EC-C18 for having fewer phenolic groups than EGCG-C18.

2.2. In vitro evaluation of the antiviral efficacy of drugs against SARS-CoV-2

EGCG, EGCG-C6, EGCG-C10, EGCG-C18, EdV-C18, and EC-C18 were tested in an initial screening by treating Vero E6 cells before and after the infection to investigate their antiviral activity against SARS-CoV-2 (Fig. 2, Method A). As no profound modifications of the entry process of SARS-CoV-2 were described from the onset of the pandemic to date, we limited our analysis to the early prototipic european strain (B.1).

Supernatants were collected 24 and 48 h post-infection (hpi) for viral genome extraction and quantification by real-time PCR. As shown in Fig. 3, EGCG, EGCG-C6, and EdV-C18 did not reduce the replicative capacity of SARS-CoV-2 even at the higher concentrations tested (80 μM).

However, the viral load, expressed as viral copies per ml of supernatant (cp/ml), was reduced by EGCG-C10 and more by EGCG-C18. The 50% inhibitory concentration (IC_{50}) was calculated 48 h after infection (hpi). EGCG-C18 and EGCG-C10 inhibited SARS-CoV-2 with IC_{50} of 5.6 $\pm$ 2.6 μM and 33 $\pm$ 4 μM μM, respectively. Interestingly, EC-C18 shows poor ability to inhibit SARS-CoV-2 replication, with a very high IC_{50} of 6937 $\pm$ 7 μM.

As a significant reduction in SARS-CoV-2 infection was observed when EGCG-C18 was added both before and after virus inoculation (Fig. 2, Method A), a second series of experiments was designed to clarify whether the most active compound more effectively prevents viral entry or replication. To determine if it interferes with the early stages of RNA replication/translation and/or the late stages of virus assembly/secretion, the administration of EGCG-C18 was performed only after viral infection (Fig. 2, Method B); in this case, no changes in the viral titer were observed compared to untreated cells; these findings indicated that EGCG-C18 does not interfere with SARS replication inside cells but acts by preventing the virus from entering the cell. It may achieve this by specifically interacting with a viral target to block entry into the host cell, or by interacting with the cell membrane to hinder the virus's ability to enter. To clarify this point, we investigated whether the compound has a direct virucidal effect by incubating the virus with EGCG-C18 before administering the mixture to the cells. (Fig. 2, Method C). Again, no antiviral activity was registered, indicating that these compounds do not exhibit virucidal activity against SARS-CoV-2; altogether these results show that EGCG-C18 prevents the SARS-CoV-2 entry by acting as a membrane-targeting drug, in contrast to what was reported for EGCG [37], where a pronounced virucidal effect upon pre-incubation with the virus suggested that SARS-CoV-2 surface proteins are major targets of EGCG.

These results underscore the significant influence of the lipophilic chain on the antiviral effect exhibited by compounds in the EGCG derivatives group. The elongation of the saturated alkyl group attached to the molecule reduces the IC_{50}, likely because it facilitates a more

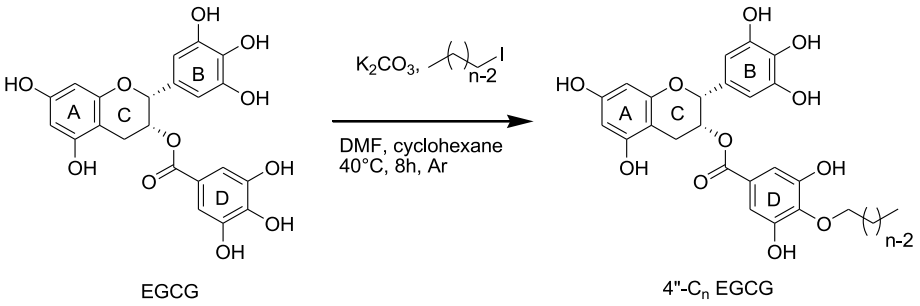

Scheme 1. Synthetic route for 4″-alkyl EGCG derivatives, where n = 6, 10 and 18.

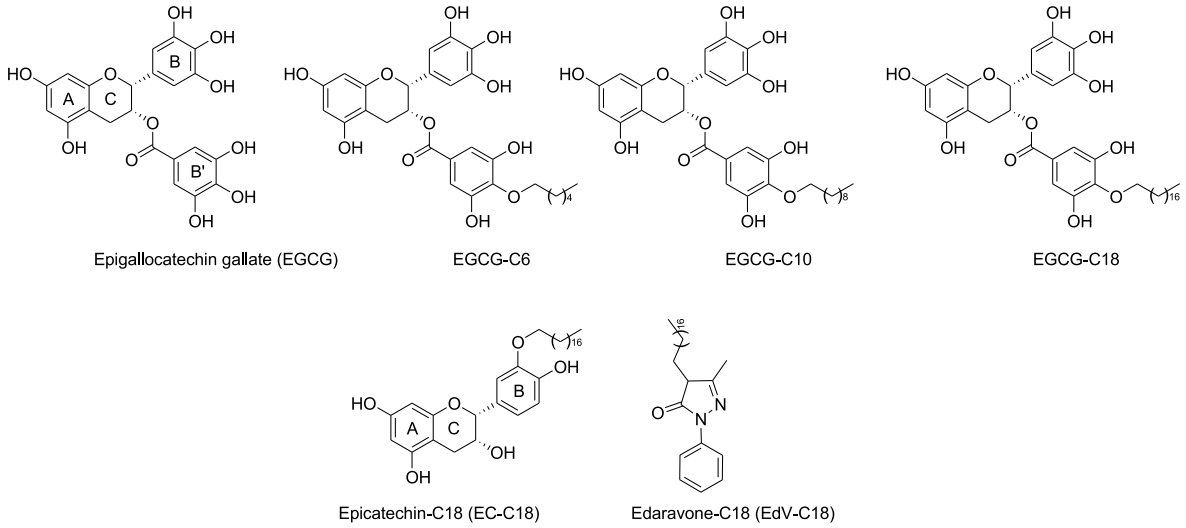

Fig. 1. Compounds tested for their antiviral properties.

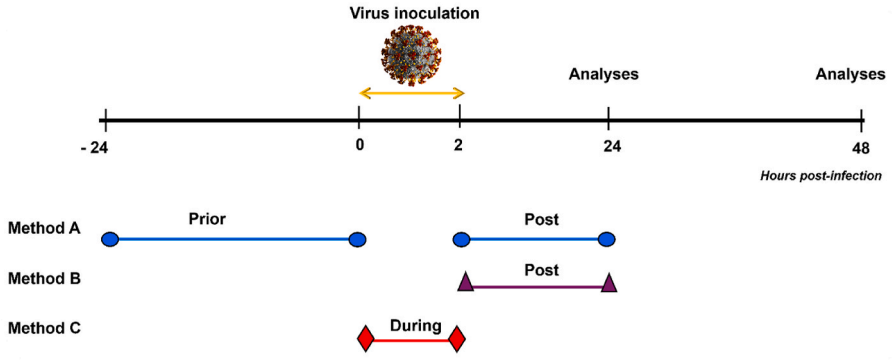

Fig. 2. The different EGCG-C18 administration methods used in this study.

effective anchoring within the cell membrane, presumably at the site of lipid rafts, where the fatty-acid side chains of the phospholipids are more saturated than those in the surrounding membrane. The inhibition data of SARS-COV-2 replication concerning EdV-C18 and EC-C18 indicate that the polyphenolic moiety of EGCG-C18 cannot be substituted without diminishing or losing the antiviral potential; interestingly, EGCG-C18 and Eda-C18 show the same affinity for PC liposomes employed as disordered (liquid-crystalline) lipid phases membrane model [34,36]. Consequently, we hypothesize that the distinctive molecular structure of lipophilic EGCG, characterised by a high number of phenolic hydroxyl groups, allows for a more efficient and selective interaction at the level of the ordered lipid phases of lipid rafts, which are characterised by a more complex composition and the presence of glycosylated lipids, enabling the formation of strong hydrogen bonds. To demonstrate the safety of EGCG-C18, its cytotoxicity was assessed in Vero-E6 and non-modified human dermal fibroblast (HDF) cells using the same Method A as the antiviral assays (see Fig. S1 in the supporting information). In Vero-E6 cells, neither compound reduced viability at 0–100 μM. In HDF cells, a modest decrease in viability (12–15%) was observed only at 100 μM for both compounds. Given that the EGCG-C18 IC50 against SARS-CoV-2 is 5.6 μM, antiviral activity occurs at concentrations well below those causing cytotoxicity in normal cell types, indicating antiviral efficacy without detectable cytotoxic effects under the tested conditions.

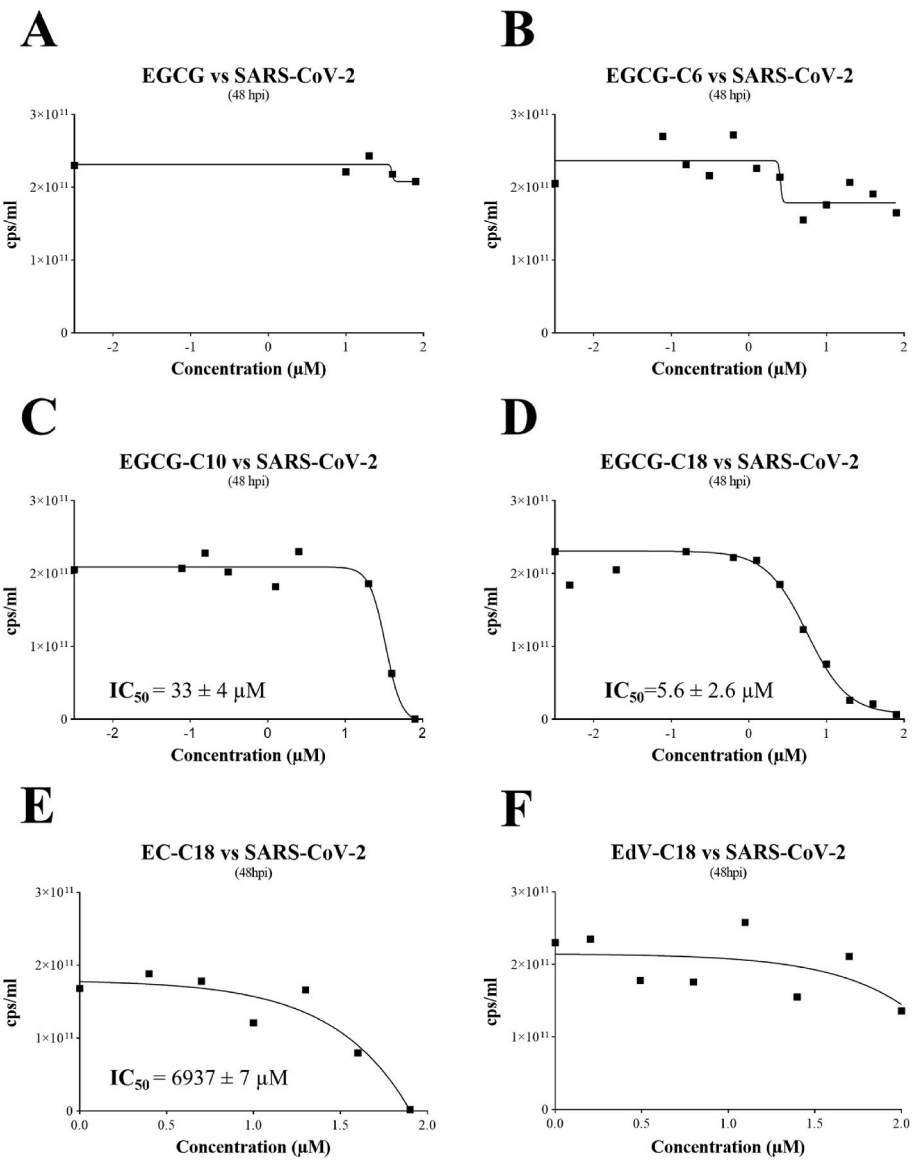

Fig. 3. Inhibition of SARS-COV-2 replication in Vero-E6 cells due to EGCG (A), EGCG-C6 (B), EGCG-C10 (C), EGCG-C18(D), Epicatechin-C18 (E) and Edaravone-C18 (F). Vero-E6 cells were pre-treated with serial dilutions of the compounds in triplicate for 24h. Cells were infected with 100 $TCID_{50}$/50 μl of SARS-CoV-2 viral stock. The infected cells were treated with compounds. Supernatants were collected 48 hpi for viral quantification by Real-Time PCR using an international standard. Experiments were independently repeated three times, and each data point represents the mean of triplicates. The IC_{50} values were calculated by nonlinear regression analysis using GraphPad Prism software.

2.3. Interaction of EGCG-C18 with lipid membrane: a combined experimental and in silico approach

To investigate the cell localization of EGCG-C18, we first employed FTIR and Raman microspectroscopies to demonstrate the presence of EGCG-C18 in the context of the cell membrane. These two techniques are mutually complementary because of their different physical origin. The IR absorption process is sensitive to polar and antisymmetric group vibrations, while Raman scattering is sensitive to polarizable and symmetric group vibrations. Hence, when combined, these techniques can provide a more complete analysis of the biological specimen under investigation [37,38]. Moreover, FTIR and Raman microspectroscopies differ in the achievable resolution, with the former reaching ~10 μm and the latter even under 1 μm with a × 100 objective: this indicates that FTIR microspectroscopy is useful for obtaining a larger picture of the sample, while Raman microspectroscopy enables subcellular analyses [39].

Infrared spectra, pre-processed as described in Material and Methods, were integrated under the following spectral intervals: 2991-2820 cm^{-1} (lipids, LIP); 2991-2949 cm^{-1} (methyl groups, CH_3); 2949-2883 cm^{-1} (methylene groups, CH_2); 1711-1485 cm^{-1} (proteins, PRT); CELL is the sum of the integrated areas in the regions 2991-2820 cm^{-1} and 1760-946 cm^{-1}. The values of the integrated areas were then used to calculate specific band area ratios (Fig. 4).

The band area ratios LIP/CELL and LIP/PRT, representing respectively the total amount of lipids within the cell and the total amount of lipids with respect to proteins, showed a similar trend, with a significant increase in the groups treated with C18, confirming the incorporation of this compound within cells. Consistently, the groups treated with C18 showed a significant increase in the CH_2/CH_3 band area ratio, which represents the length of the aliphatic chains.

Fig. 5 presents the microphotographs of representative single cells, the Raman maps obtained as previously described, and a representative Raman spectrum collected from the lipid-rich area of the cell. All experimental groups exhibited distributions of lipids consistent with their known localization in the cytoplasmic membrane. In the EGCG-

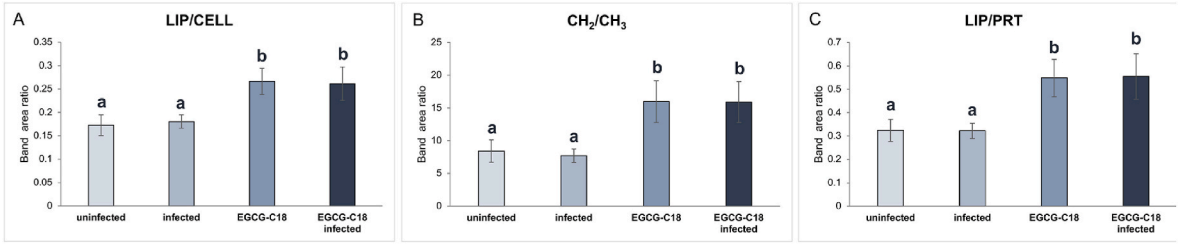

Fig. 4. Statistical evaluation of the biochemical composition of the experimental groups in terms of: (A,C) lipids (LIP/CELL and LIP/PRT), (B) length of aliphatic chains (CH_2/CH_3). (Data are reported as mean ± SD. Different letters indicate statistically significant differences among groups ($p < 0.05$; one-way ANOVA and Tukey's multiple comparisons test).

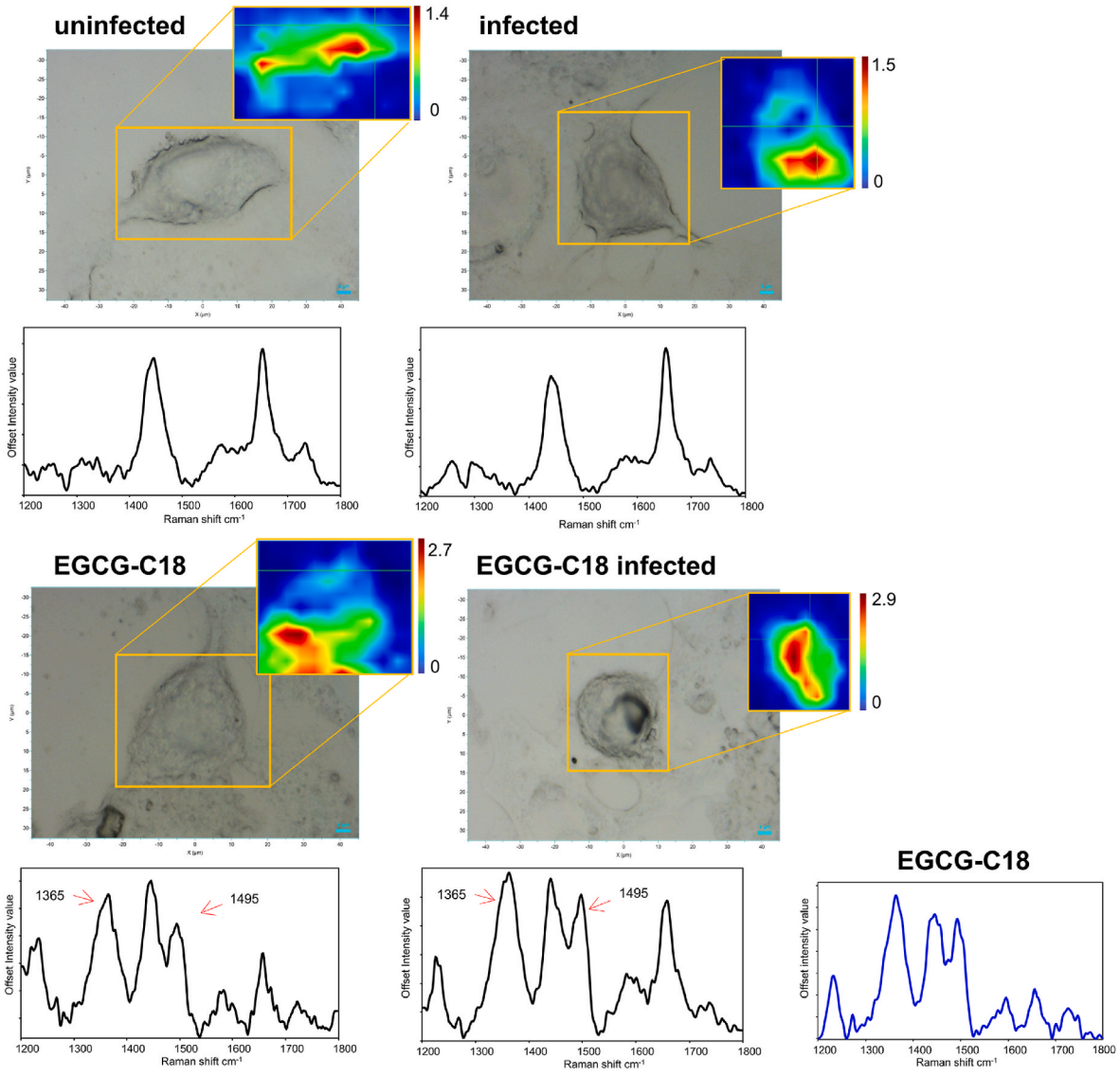

Fig. 5. Raman mapping analysis of representative single cells from the experimental groups. Photomicrographs reporting the selected cells and overlapping false color maps showing the topographical distribution of lipids (black/blue corresponds to the lowest values, green intermediate, and red/dark red to the highest ones). Representative Raman spectra were extracted from lipid-rich areas. The spectrum of pristine EGCG-C18 is reported in blue. (For interpretation of the references to color in this figure legend, the reader is referred to the Web version of this article.)

C18 infected and uninfected groups, Raman spectra extracted from lipid-rich areas reveal some peculiar spectral features found in the Raman spectrum of pristine EGCG-C18, demonstrating a co-localization of EGCG-C18 with particularly abundant lipid quantities, presumably corresponding to lipid rafts.

Starting from the experimental evidence [28,40,41] that the natural EGCG preferentially binds with cell membranes in the lipid raft regions, we hypothesized that the polyphenol structure confers to EGCG-C18 a potential ability to interact with glycosylated lipids present in these domains, in particular GM1. For this purpose, we conducted an in silico

study of the interaction of both EGCG and EGCG-C18 with GM1, which plays a crucial role in clustering cellular membrane glycoproteins after the binding of viruses and is thus vital for their infectivity. A lipid raft model was created based on the composition reported in the current literature [42]. GM1 was inserted into the lipid raft membrane, while EGCG and EGCG-C18 molecules were added in the water phase, to mimic the experimental conditions better. In all lipid raft models, Chol acted as a sort of spacer between the hydrocarbon chains of the sphingolipids, keeping the raft assembly together behaving like a glue, with this behaviour maintained throughout each MD time.

The EGCG interacted very quickly with the polar part of the membrane, interposing itself between the polar heads of lipids and the sugar portion of GM1 (Fig. 6). The catechin will maintain this position throughout the entire simulation duration, demonstrating a robust interaction at the water-lipid interface. To confirm this, the distance of EGCG from the lipid surface was monitored from the beginning to the end of the MD simulation. The analysis revealed that the distance between catechin and the polar heads of lipid rafts was less than 0.2 nm (Fig. 6B), indicating high stability and a clear propensity for the molecule to remain in the specified position.

Concerning EGCG-C18, the aliphatic chain promotes the interaction with GM1. During the MD simulation, the catechin derivative alternated its use of the head and tail in the interaction with the sugar portion of GM1, also inducing a degree of mobility in the sugar components (Fig. 7).

Moreover, continuing to fluctuate at the proximity of GM1, in the last 50 ns of simulation the tail of the EGCG-C18 was arranged to move the Chol residues apart, leading to an evident switch of a PSM molecule from GM1 and then generating a small cavity close to the GM1 (Fig. 7E and F) that is absent in the simulation with EGCG. Overall, a very high level of stability has been observed, and the chain of EGCG-C18 strongly interacts with GM1 throughout all the MD trajectory, and the Chol residues that packs around the catechin derivative turned to behave like a glue for the raft (Fig. 8).

Based on the lipid shifting effect induced by the catechin derivative and the EGCG-C18's strong ability to interact with GM1, the computational results indicate a likely intercalation of the drug within the lipid raft medium, leading to the consequent perturbation of the domains. Interestingly, analogous simulations performed on unsaturated systems, such as oleyl- and linoleoyl-containing EGCG derivatives, did not show stable interactions with GM1-enriched lipid raft domains (data not shown).

2.4. *Effect of SARS-CoV-2 infection and EGCG-C18 treatment: GM1 modulation*

The ability of SARS-CoV-2 to induce receptor clustering at the cell surface is essential for its infectivity and internalization, with lipid microdomains playing a pivotal role as platforms where receptors are concentrated and can interact with the viral spike protein [7,15–17,43]. The FTIR and Raman microspectroscopy confirmed that EGCG-C18 incorporates into the plasma membrane, while in silico simulations indicated a strong interaction of EGCG-C18 with GM1 within a membrane environment, potentially altering the organization of lipid rafts. Given that GM1 has been described as an additional entry point for SARS-CoV-2 [44] and acts directly as a cofactor for binding SARS-CoV-2 to the cell membrane [23,45], the observed reduction in viral infection due to the EGCG-C18 treatment (see Fig. 3D) may be directly related to this interaction. Therefore, we employed fluorescently labeled cholera toxin subunit B (CTxB) to assess GM1 levels on the cell membrane by means of flow cytometry and confocal microscopy, as these are widely used methods to probe GM1 distribution and organization [46–49]. However, we acknowledge that the binding of CTxB to GM1 is highly dependent on the molecular context of the membrane—including factors such as glycolipid composition, membrane order, cholesterol content, and the presence of interacting compounds [50,51] like EGCG-C18. To address this, we included appropriate controls in our experiments, such as cells treated with EGCG-C18 alone, untreated cells, and cells infected with SARS-CoV-2. These controls allowed us to interpret the fluorescence signals as indicative of the accessible or "recognizable" GM1 pools on the cell surface under our specific experimental conditions, rather than a direct quantitative measure of total GM1 levels on the cell surface. Firstly, we assessed changes in GM1 expression following SARS-CoV-2 infection by measuring fluorescence of labeled CTxB. As shown in Fig. 9A, GM1-associated fluorescence increases by approximately 48% at 24 h post-infection (Fig. 9A). This significant increase in fluorescence likely indicates a cellular response to viral infection—potentially involving enhanced GM1 clustering or accessibility—thus facilitating viral entry into the host cells.

Subsequently, GM1 levels were analyzed in infected and uninfected cells pre-treated with EGCG-C18 for 24 h. In the uninfected cells, treatment with EGCG-C18 did not result in any significant change in

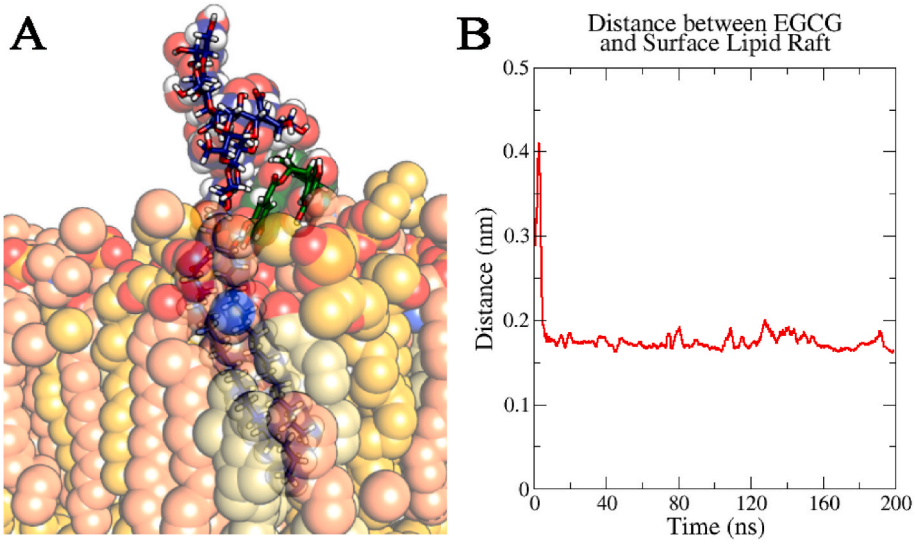

Fig. 6. Representative structure of the EGCG (green) between the sugar part of GM1 (blue) and the lipid raft (Chol, GM1, and POPC are highlighted in beige, gold, and coral, respectively) (A). Monitored distance between EGCG and Surface Lipid Raft (B). (For interpretation of the references to color in this figure legend, the reader is referred to the Web version of this article.)

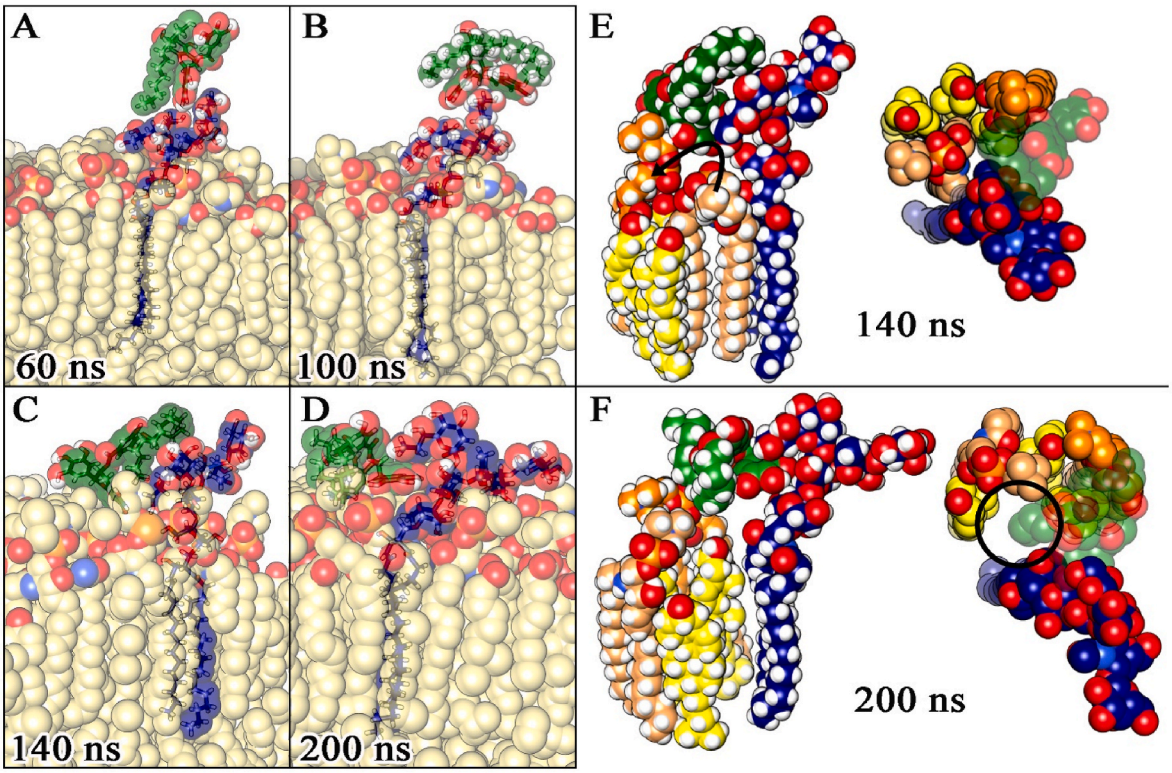

Fig. 7. Dynamical behaviour of the EGCG-C18 within the lipid raft at 60 ns (a), 100 ns (b), 140 ns (c), and 200 ns (d). Front and top views of the EGCG-C18 induced lipid shifting effect (e, f). Chol, PSM, POPC, GM1, and EGCG-C18 are colored yellow, coral, orange, blue, and transparent green, respectively. The arrow and the circle highlight the switch of the PSM residue and the resulting empty space in the lipid system. (For interpretation of the references to color in this figure legend, the reader is referred to the Web version of this article.)

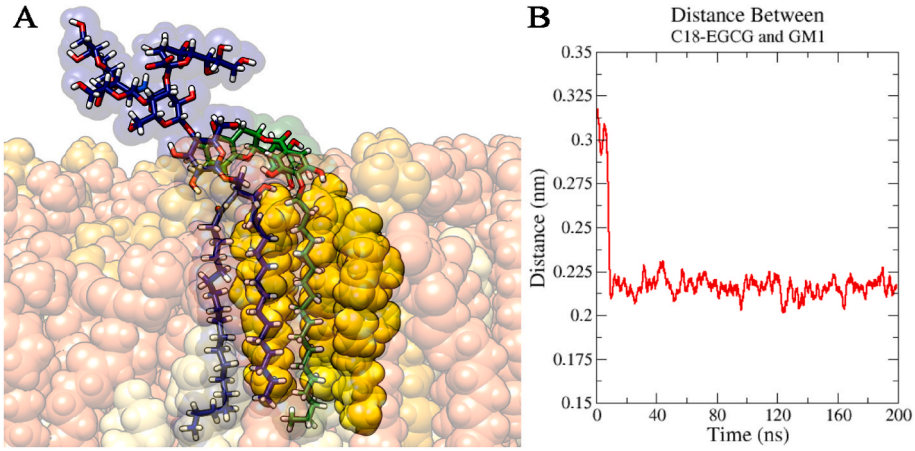

Fig. 8. Representative structure of EGCG-C18 (green) in contact with GM1 (blue), and the three proximal Chol Molecules (yellow). The lipid raft is reported in transparent surface, and the Chol, PSM, and POPC, are colored in yellow, coral, and orange, respectively. (For interpretation of the references to color in this figure legend, the reader is referred to the Web version of this article.)

GM1 levels. By contrast, pre-treatment with EGCG-C18 led to a dramatic reduction in GM1 fluorescent signal in the infected cells, decreasing it by 42% compared to untreated cells, and restoring GM1 levels to those observed in the absence of infection (106% vs. 100%, respectively) (Fig. 9A). Therefore, EGCG-C18 could directly impact the GM1 organization or the membrane order of cell membrane of infected cells which prevents the virus from entering cells. In these experimental settings, experiments conducted with EGCG demonstrated that this compound, interestingly, had no impact on the ability of CTxB to bind to GM1 in either infected or uninfected cells.

The selective effect observed for EGCG-C18 highlights its potential advantage as a membrane-targeting antiviral: it can restore GM1 levels in infected cells while leaving uninfected cells largely unaffected. This targeted approach minimises potential side effects and helps maintain the integrity of membrane in uninfected cells, making it a promising option for effective therapy.

To visualize the localization of GM1 within the cells, confocal microscopy was performed in parallel with the same experimental conditions analyzed by flow cytometry (Fig. 9C). The trend of fluorescent intensity overlaps with that described by flow cytometry. As seen in the left panel of the figure, the uninfected cells exhibited a lower signal for GM1 (FITC-green) compared to the infected cells in all three conditions

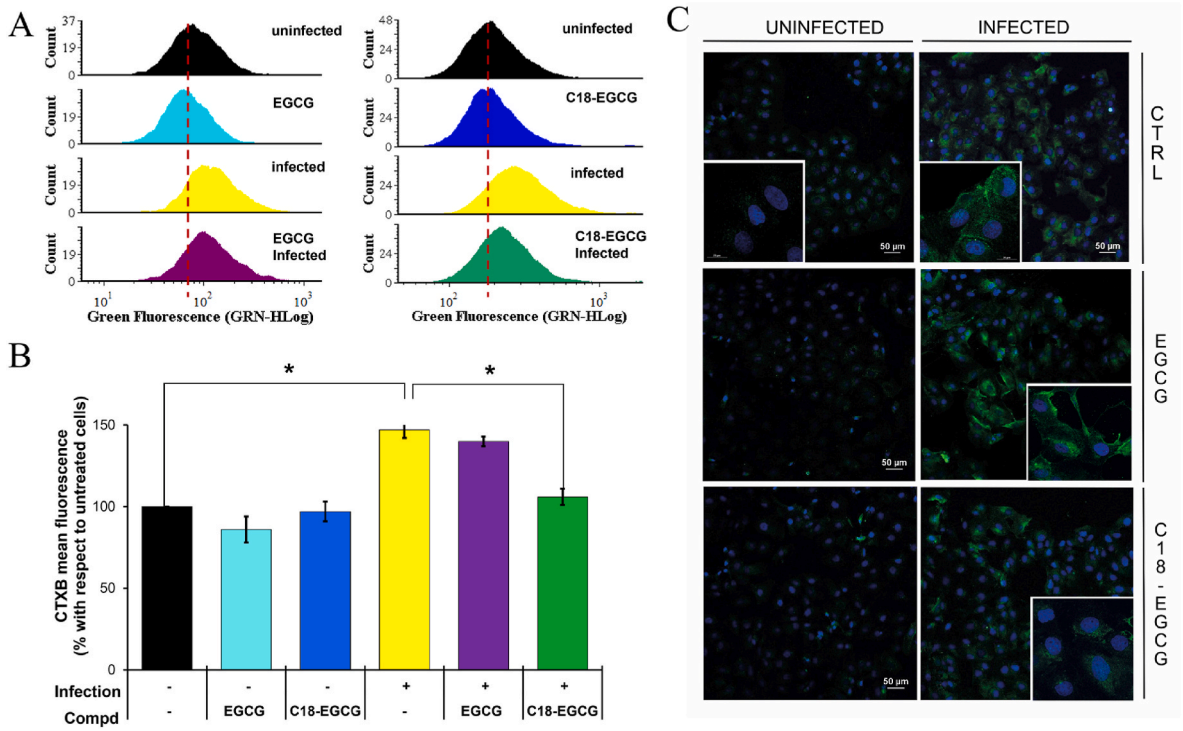

Fig. 9. Quantification of GM1 expression on the membrane of Vero-E6 cells by flow cytometry and confocal microscopy. GM1 levels in cells with or without SARS-CoV-2 infection, pretreated or not with EGCG and EGCG-C18 measured at 24-h post-infection. **(A–B)** After trypsinization, cells were incubated with CTxB-FITC (1.0 μg/mL) in PBS for 30 min and fixed with 2% PFA for 10 min at rt before the analyses. Top: representative FACS (fluorescence-activated single-cell sorting overlay plots) obtained from flow cytometry depicting GM1 level; down: histograms showing the CTxB mean fluorescence. **(C)** Confocal microscopy allows the visualization of the subcellular localization of GM1 (green) in cell culture (nuclei in blue). The data is the mean of triplicated experiments ±SD. *$p < 0.05$. (For interpretation of the references to color in this figure legend, the reader is referred to the Web version of this article.)

examined (Fig. 9C right panels). In CTRL infected cells, where GM1 is more evident, the staining pattern is diffuse and present both in the plasma membrane and the cytoplasm. The EGCG-treated cells did not show any significant alteration upon infection compared with CTRL, neither in intensity levels nor in signal distribution. In the presence of EGCG-C18, the fluorescent intensity was lower compared with EGCG, and the staining pattern was primarily localised in the cytoplasm and suggestive of a perinuclear localization (more clearly visible in the inset).

2.5. *Effect of EGCG-C18 pre-treatment on EGFR activation in SARS-CoV-2 infected cells*

The epidermal growth factor receptor (EGFR), a transmembrane glycoprotein and member of the receptor tyrosine kinase (RTK) family, plays a crucial role in various cellular processes. Activation of wild type EGFR occurs when ligands such as EGF bind to its extracellular domain, leading to receptor dimerization that activates its cytoplasmic tyrosine kinase domain. This activation phosphorylates tyrosine residues, triggering multiple downstream signaling pathways, which are essential for cancer progression [52] and viral infections [53].

It has been shown that the S1 and RBD domains of the S protein of SARS-CoV-2 induced EGFR activation promoting EGFR phosphorylation

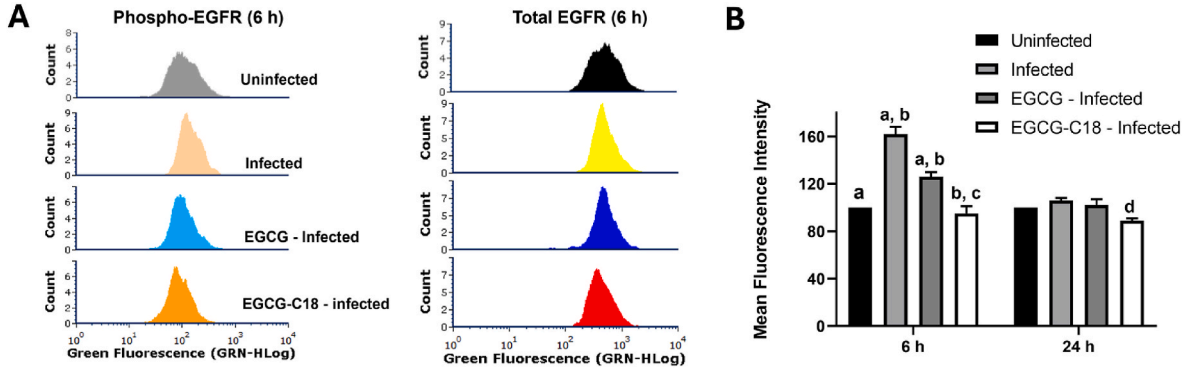

Fig. 10. Effect of C18-EGCG and EGCG on the EGFR activation by flow cytometry. Cells were pretreated with EGCG-C18 (5 μM) and EGCG (20 μM) for 24 h, followed by SARS-CoV-2 infection. Flow cytometry analyses were performed after 6 h and 24 h post-infection. (A) Representative FACS cytograms showing levels of phospho-EGFR and total EGFR after 6 h post-infection. (B)Bar graphs representing the percentage of EGFR activation normalized to uninfected cells expressed as the ratio phospho-EGFR/EGFR. a, b, c, d: $p < 0.05$.

[54].

In line with the existing literature [53,55,56], our data presented in Fig. 10 demonstrate that SARS-CoV-2 infection leads to a significant increase in EGFR phosphorylation at Tyr1068 (Y1068), resulting in enhanced receptor activation, particularly within the first 6 h following infection (62% more than in uninfected cells). After 24 h, the levels of phosphorylated EGFR return to baseline, confirming that activated EGFR may play a role during the viral entry into host cells [53].

To gain a deeper understanding of the mechanism of action of EGCG-C18, we assessed the effects of pre-treatment with EGCG and EGCG-C18 on EGFR activation following 6 and 24 h of SARS-CoV-2 infection. As illustrated in Fig. 10, pre-treatment with both compounds reduced EGFR phosphorylation at 6 h post-infection, although with different efficacy. EGCG-C18 demonstrated greater effectiveness, bringing the phospho-EGFR/EGFR ratio close to baseline levels observed in uninfected cells (96% compared to 100%). In contrast, EGCG reduced EGFR phosphorylation from 162% in infected cells to 129%. This is not surprising, as EGCG is a natural compound well-known for binding the cytoplasmic tyrosine kinase domain of EGFR, inhibiting its activation through an ATP-competitive mechanism [57,58]. Several studies have shown that EGFR activity can be modulated by its surrounding lipid environment. Since EGCG-C18 primarily localizes in the cellular membrane (Fig. 5) and modulates the organization of GM1 (Fig. 9), its capacity to reduce EGFR activation likely results from mechanisms related to its membrane-targeting properties. Future research should investigate whether this derivative affects the distribution or function of other membrane-associated lipids. For example, ganglioside GM3—but not GM1—has been shown to inhibit EGFR activation through direct interaction [59]. Therefore additional experiments could elucidate other mechanisms by which this compound modulates EGFR signaling in cells infected with SARS-CoV-2.

2.6. *In vitro evaluation of the antiviral efficacy of drugs against HIV, Herpes Simplex, and influenza B viruses*

As a membrane and LR targeting drug, EGCG-C18 could potentially exhibit antiviral properties against a wide spectrum of enveloped and non-enveloped viruses. Indeed, although the steps immediately preceding the membrane fusion process are the most influenced by lipid raft rearrangement, non-enveloped viruses also exploit cell membrane glycoprotein clustering through complex interactions among lipid raft components. To explore the compound's antiviral activity spectrum, various experiments were set up to quantify its inhibitory effects on infections by different enveloped viruses: Herpes Simplex type 1, Influenza B, and HIV-1. Each of these viruses was titered as described and used to challenge tissue culture cells: U87/CXCR4 for HSV-1 and HIV-1, MDCK for influenza B. Method A was used for the challenge with all three viruses. IC_{50} was calculated 48 h after infection and reported in Fig. 11. Although with different efficacy (for example, IC_{50} against HIV-1 was 5-fold higher than against influenza B: 35 ± 4 vs 7 ± 3 μM), EGCG-C18 demonstrated significant broad-spectrum antiviral activity against enveloped viruses, consistent with an effect on lipid raft–associated processes.

2.7. *ADMET/drug-likeness prediction for EGCG-C18*

To obtain preliminary insight into the pharmacokinetic, toxicological, and drug-likeness profile of the synthesized compound, in silico ADME–tox predictions were performed (Fig. 12) using the ADMET AI platform, a machine-learning–based approach commonly applied in early drug discovery to support the assessment of pharmacokinetic behavior and safety liabilities prior to experimental evaluation [60]. The full prediction panel is reported in the Supplementary Materials.

The predicted physicochemical and ADME properties indicate a highly lipophilic compound with multiple deviations from classical drug-likeness rules. According to Lipinski's rule of five, EGCG-C18 satisfies only one of the five criteria [61]. The high molecular weight (708.89 Da), elevated LogP (9.83), and large topological polar surface area (TPSA = 177.14 $Å^2$) suggest limited passive diffusion across biological membranes and very low aqueous solubility, as commonly observed for compounds outside conventional drug-like chemical space [61]. Despite these characteristics, the predicted human intestinal absorption (0.97) and moderate oral bioavailability (0.45) indicate that absorption may still occur, likely driven by partitioning into lipid bilayers rather than classical passive permeability mechanisms. The relatively low PAMPA permeability (0.32) combined with high predicted intestinal absorption and pronounced lipophilicity is consistent with preferential association with lipid membranes and slow desorption, highlighting the compound's potential for membrane-targeted delivery [61]. In silico metabolism predictions indicate that EGCG-C18 is primarily cleared via CYP3A4-mediated pathways, with a high probability of being a CYP3A4 substrate (0.81; 89th percentile) and elevated intrinsic clearance in hepatocyte and microsomal models. Inhibition of other major CYP isoforms is generally low, although moderate CYP3A4 inhibition (0.34; 74th percentile) suggests a potential for drug–drug interactions under high exposure conditions [62]. Toxicity predictions suggest an overall favorable safety profile, with low probabilities for clinical toxicity, mutagenicity, carcinogenicity, acute toxicity, endocrine disruption, and skin reactivity (see Supplementary Material). However, the predicted hERG blocking potential (0.81; 79th percentile) represents a possible safety concern that should be evaluated experimentally due to cardiotoxicity risk [63]. Overall, the predicted ADME profile suggests pharmacokinetics governed by extensive tissue and membrane sequestration combined with rapid metabolic clearance upon hepatic exposure. The strong tendency for membrane and lipid-domain partitioning supports its suitability for lipid-focused targeting

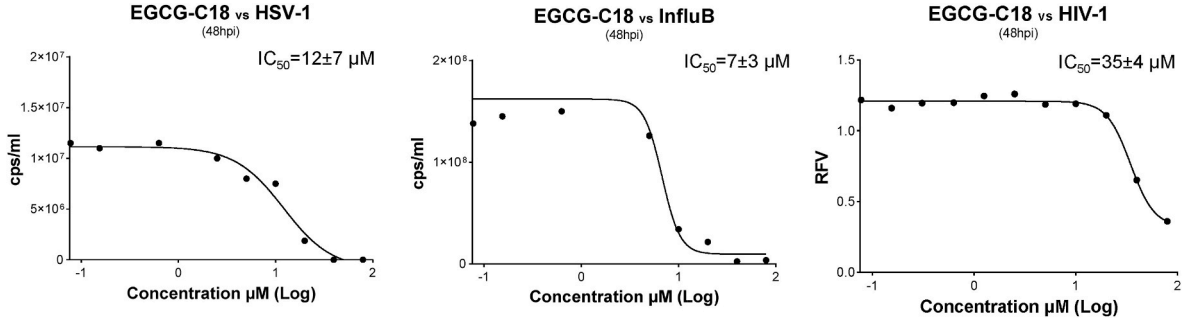

Fig. 11. Inhibition of HSV-1 and HIV-1 replication in U87/CXCR4 cells and FluB in MDCK cells due to EGCG-C18. Cells were pre-treated with serial dilutions of EGCG-C18 in triplicate for 24h. Cells were infected with viral stocks and treated with the compound. Supernatants were collected 48 hpi for viral quantification by Real-Time PCR. Experiments were independently repeated three times. Each point represents the mean. The IC_{50} was calculated using nonlinear regression analysis of GraphPad Prism software.

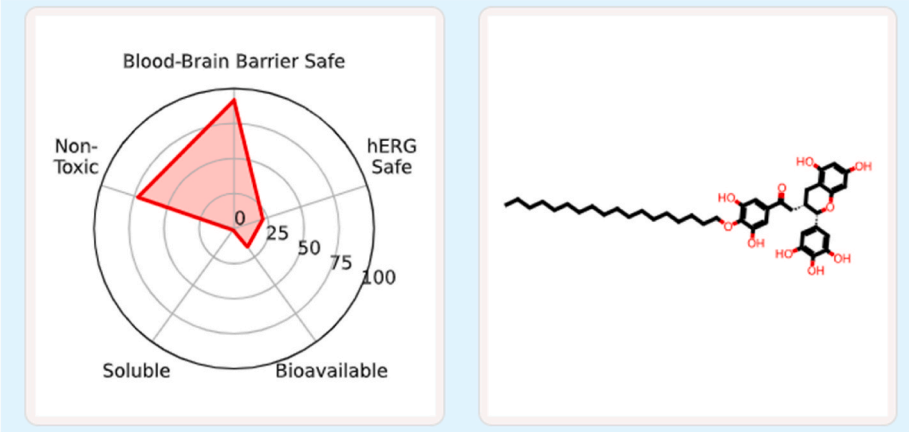

Fig. 12. ADME in silico prediction for EGCG-C18: a radial plot is shown summarizing five key ADMET properties in terms of their DrugBank percentile. Blood-Brain Barrier Safe: The probability that the molecule does not cross the blood-brain barrier; hERG Safe: The probability that the molecule does not block the human ether-a-go-go (hERG) channel; Bioavailable: The probability that the molecule is orally bioavailable; Soluble: The aqueous solubility of the molecule, Non-Toxic: The probability that the molecule would not show clinical toxicity.

approaches but the extremely low predicted aqueous solubility (log S = −6.95) represents a major biopharmaceutical limitation for its translational feasibility. All these findings highlight the importance of formulation strategies for highly lipophilic compounds in modulating systemic exposure and support the potential suitability of lipid-based delivery approaches including liposomes, solid lipid nanoparticles, and raft-mimetic vesicles.

3. Conclusions

In this study, we synthesized a series of lipophilic derivatives of EGCG. The amphiphilic molecules were obtained through the introduction of saturated carbon chains of various lengths (6, 10, and 18 Carbon atoms), bound to the skeleton of EGCG by an ether bond. Eda-C18 and Epicatechin-C18 were added to investigate the influence of the drug's hydrophilic portion on counteracting virus entry. The therapeutic potential of the molecule pool has been assessed in terms of inhibiting SARS-Cov-2 replication in Vero-E6 cells, and EGCG-C18 proved to be most effective in exerting a preventive effect. We hypothesized that, owing to its peculiar amphiphilic structure, characterised by a long C18 chain and multiple hydroxyl groups, the EGCG derivative could interact with cellular membranes, possibly within lipid raft–enriched domains, and alter their lipid organisation. Such changes could, in turn, interfere with the virus internalization process.We demonstrated the localization of the lipophilic polyphenol within a lipid-rich area of the cell membrane using Fourier Transform Infrared and Raman Microspectroscopy; through Molecular Dynamics simulation, flow cytometry, and confocal microscopy, we evidenced that EGCG-C18 interacts with GM1 present in the lipid rafts and that pre-treatment of infected cells with EGCG-C18 resulted in a dramatic reduction in GM1 expression, restoring its levels to those observed in the absence of infection. We also showed that pre-treatment reduced EGFR phosphorylation at 6 h post-infection, bringing the phospho-EGFR/EGFR ratio close to baseline levels observed in uninfected cells. The action of EGCG-C18 as a membrane-targeting and broad-spectrum antiviral drug has been corroborated by demonstrating the antiviral effect against various viral infections, such as Herpes Simplex virus, Influenza B, and HIV-1.

4. Experimental section

4.1. Synthetic procedure

The materials and reagents used in the synthetic procedures were purchased from Sigma Aldrich Co. (Stenheim, Germany) and used without purification. All solvents were analytically pure and dried before use. TLC was carried out on aluminium sheets precoated with silica gel 60 F254 (Merck). Column chromatography was performed using silica gel 60 (230–400 mesh). High-resolution MS (HRMS) ESI analyses were performed on a Xevo G2-XSQTof (Waters) mass spectrometer. Mass spectrometric detection was performed in the negative ion mode. The ^{1}H and ^{13}C NMR spectra were recorded at 400 and 100 MHz, respectively, on an Agilent Technologies 400 MHz Premium Shielded spectrometer. Chemical shifts (δ) are reported in ppm relative to TMS and coupling constants (J) in Hz. EGCG-C6, EGCG-C10, EGCG-C18, and Edaravone-C18 were obtained as previously described [34,36,64].

EGCG-C6. ^{1}H NMR (Acetone-d6, 500 MHz): $\delta = 0.87$ (t, $J = 7.0$ Hz, 3H), 1.25-1.34 (m, 4H), 1.36-1.44 (m, 2H)), 1.67-1.74 (m, 2H), 2.95 (dd, $J = 2.8$, $J = 17.2$ Hz, 1 H), 3.04 (dd, $J = 4.3$ Hz, $J = 17.2$ Hz, 1 H), 4.08 (t, $J = 7.0$ Hz, 2 H), 5.07 (bs, 1H), 5.49 (bs, 1H), 6.02 (d, $J = 2.3$ Hz, 1H), 6.04 (d, $J = 2.3$ Hz, 1H), 6.65 (s, 2H), 7.03 (s, 2H) ^{13}C NMR (Acetone-d6, 125 MHz): ^{13}C NMR (Acetone-d6, 125 MHz): $\delta = 14.3$, 23.3, 26.2, 26.6, 30.6, 32.4, 69.7, 73.5, 78.0, 95.9, 96.6, 99.0, 106.7, 110.0, 126.2, 130.7, 133.2, 139.6, 146.4, 151.1, 157.1, 157.5, 157.9, 165.9. Relative NMR purity >98% ESI-MS: (*m/z*.) 543.19 [M+ 1].

EGCG-C10: ^{1}H NMR (Acetone-d6, 500 MHz): $\delta = 0.88$ (t, $J = 7.0$ Hz, 3H),1.21-1.35 (m, 12H), 1.36-1.47 (m, 2H), 1.67-1.78 (m, 2H), 2.97-3.09 (m, 2H), 4.05-4.15 (m, 2H), 5.07 (bs, 1H), 5.38 (bs, 1H), 6.05 (s, 2H), 6.69 (s, 2H), 7.07 (s, 2H). ^{13}C NMR (Acetone-d6, 125 MHz): $\delta =$ 14.4, 23.3, 26.3, 26.6, 30.8, 32.6, 70.4, 73.3, 78.3, 95.9, 96.6, 98.9, 106.9, 109.9, 126.2, 130.5, 133.4, 139.6, 146.6, 151.4, 157.1, 157.5, 157.9, 166.3. Relative NMR purity >98% ESI-MS: (*m/z*.) 599.25 [M+ 1].

EGCG-C18. ^{1}H NMR (Acetone-d6, 400 MHz): $\delta = 0.87$ (t, $J = 6.8$ Hz, 3H), 1.23-1.32 (m, 28H, overlapping), 1.34-1.45 (m, 2H), 1.67-1.76 (m, 2H), 2.97 (dd, $J = 2.4$ Hz, $J = 13.9$ Hz, 1H), 3.03 (dd, $J = 3.9$ Hz, $J =$ 13.9 Hz,1H), 4.07 (t, $J = 7.0$ Hz, 2H), 5.07 (bs, 1H), 5.52 (bs,1H), 6.01 (d, $J = 2.3$ Hz, 1H), 6.03 (d, $J = 2.3$ Hz, 1H), 6.64 (s, 2H), 7.01 (s, 2H). ^{13}C NMR (Acetone-d6, 100 MHz): $\delta = 14.4$, 23.3, 26.4, 26.6, 32.6, 70.0, 73.3, 78.1, 95.8, 96.4, 98.8, 106.7, 109.8, 126.1, 130.5, 133.3, 139.5, 146.5, 151.2, 157.1, 157.4, 157.8, 166.1. Relative NMR purity >98% ESI-MS: (*m/z*.) 711.37 [M+ 1].

Edaravone-C18. ^{1}H NMR ($CDCl_3$, 400 MHz): $\delta = \delta$ 0.87 (t, $J = 6.8$ Hz, 3H), 1.14–1.37 (m, 32 H), 1.78–1.90 (m, 1 H), 1.94–2.05 (m, 1 H), 2.15 (s,3H), 3.26 (t, $J = 5.6$ Hz, 2H), 7.17 (t, $J = 7.2$ Hz, 1H), 7.39 (t, $J =$ 8.1 Hz, 2H), 7.89 (d, $J = 8.1$ Hz, 2H), 13C NMR (CDCl3, 100 MHz): δ 14.3, 16.0, 22.9, 25.6, 27.7, 29.4, 29.5, 29.7, 29.8, 32.1, 52.6, 118.9,

125.0, 129.0, 138.2, 160.2, 173.6. Relative NMR purity >98% ESI-MS: (*m/z*.) 424.7 [M − 1]$^-$.

Epicatechin-C18. Potassium carbonate (138 mg, 1 mmol, 1.5 eq) was suspended in anhydrous DMSO (5 ml), and the mixture was stirred for 15 min at 50 °C. (−)-Epicatechin (200 mg, 0.65 mmol, 1 eq) and then 1-iodooctadecane (226 μl, 0.65 mmol, 1 eq) were added to the mixture under flow of argon. The reaction was stirred for 12 h, at 50 °C. After completion, the reaction was monitored by thin-layer chromatography (silica gel) and then acidified to pH 7 with aqueous HCl. After extraction with EtOAc, the volatiles were removed under reduced pressure. The raw material was purified by silica gel column chromatography, cyclohexane-EtOAc, 94:6. The product is a white solid. Yield: 55 mg, 15 %, m.p: 100.4-101 °C. ^{1}H NMR (600 MHz, DMSO-d_6): δ 0.85 (t, J = 6.9 Hz, 3H, CH_3), 1.24 (s, 28H, CH_2), 1.37 – 1.44 (m, 2H, CH_2), 1.65 – 1.73 (m, 2H, CH_2), 2.32 – 2.39 (dd, J = 15.9 Hz, J = 7.8 Hz, 1H, CH), 2.61 – 2.68 (dd, J = 15.9 Hz, J = 5.3 Hz, 1H, CH), 3.82 (m, 1H, CH), 3.92 (t, J = 6.6 Hz, 2H, CH_2), 4.51 (d, J = 7.5 Hz, 1H, CH), 4.88 (d, J = 5.2 Hz, 1H, OH), 5.69 (d, J = 2.3 Hz, 1H, Ar–H), 5.89 (d, J = 2.3 Hz, 1H, Ar–H), 6.69 (dd, J = 8.4, 2.1 Hz, 1H, Ar–H), 6.77 (d, J = 2.1 Hz, 1H, Ar–H), 6.84 (d, J = 8.4 Hz, 1H, Ar–H), 8.80 (s, 1H, OH), 8.93 (s, 1H, OH), 9.17 (s, 1H, OH).^{13}C NMR (150 MHz, DMSO-d_6): δ 13.9, 22.1, 25.5, 28.7, 28.8, 28.9, 29.0, 31.3, 66.3, 68.4, 80.8, 93.8, 95.1, 99.0, 113.2, 114.4, 118.2, 127.3, 129.8, 132.3, 146.4, 146.4, 155.2, 156.2, 156.4. Relative NMR purity >98% ESI-MS: (*m/z*) = 541.3 [M − 1]$^-$.

4.2. Cell culture

Vero E6, U87/CXCR4 (engineered human glioma cell line), HDF (Human dermal fibroblasts) and MDCK (Dog kidney derived epithelium) cell lines were cultured in Dulbecco's modified Eagle's medium (DMEM, Euroclone, Milano, Italy) supplemented with 10% fetal bovine serum (FBS, Euroclone), 100 U/ml penicillin/streptomycin (PS, Euroclone) and 1X MEM Eagle non-essential amino acids (NEAA) (1%, v/v). The culture media of U87/CXCR4 cell lines were supplemented with geneticin (300 μg/ml) and puromycin (1 μg/ml). Cells were maintained in T25 tissue culture flasks (CELLSTAR, Greiner Bio-One, Frickenhausen, Germany) at 37 °C in 5% CO_2 and 95% humidity. For the Vero E6, U87/CXCR4 and MDCK the confluent monolayer was passed once a week (1:5) following trypsinization. The HDF cells were used at passages 4-10 and passed every 3 days (1:2).

4.3. Cell viability assay

To determine whether treatments affected viability, Vero E6, U87/CXCR4 and HDF cells were exposed to increasing concentrations (1-160 μM) of EGCG or alkylated EGCG every 24 h for an entire time of 72 h. Following treatments, 3-(4,5-dimethylthiazol-2-yl)-2,5-diphenyltetrazolium bromide (MTT) assay was performed as previously reported [65]. The 50% inhibiting concentration (IC_{50}) was determined by non-linear regression analysis with a three-parameter fit by utilizing SigmaPlot 12.0 Software, USA, Systat Software, Inc. SigmaPlot for-Windows. Each experiment was performed at least five times in triplicate.

4.4. Virus stocks

The isolation of severe acute respiratory syndrome coronavirus 2 (SARS-CoV-2, EPI_ISL_417491) was performed by infecting Vero E6 cells using RT-PCR positive nasopharyngeal swab collected at Virology Unit from Ospedali Riuniti, Ancona (Italy) as described by Alessandrini et al. [66]. Briefly, 2 × 10^6 Vero E6 cell suspension was incubated (1 h at 37 °C in 5% CO_2) with 500 μl of swab in 2 ml of complete medium. The suspension was transferred into a 25 cm^2 tissue culture flask (6 ml final volume). Three days after infection, Vero E6 cells (4 × 10^6), seeded 24 h before in 75 cm^2 flasks, were inoculated with 2 mL of the virus in a final volume of 13 mL to obtain a larger viral stock. Supernatant of the infected cells was collected three days after infection at 80% cytopathic effects (CPE), centrifuged at 1400 RCF for 10 min, filtered using 0.2 μm filter, aliquoted and stored at −80 °C. The isolation of Herpes Simplex Virus type 1 (HSV-1) and Influenza B (Flu B) were performed, as described above, by infecting U87/CXCR4 and MDCK cells respectively, using RT-PCR positive bronchoalveolar lavage (BAL) collected at Virology Unit from Ospedali Riuniti, Ancona (Italy). The supernatant of HIV plasmid transfection (pNL4-3) containing infectious viruses was used as HIV-1 virus stock to infect U87/CXCR4 cells [67].

4.5. Titration of virus stocks

To determine the 50% tissue culture infectious dose ($TCID_{50}$) of the viral stocks, 50 μl of ten-fold serial dilutions in culture media (ranging from 10^{-1} to 10^{-8}) for virus stocks (SARS-CoV- 2, HSV-1 and Flu B) were incubated with cells (seeded 24 h before in 96-well microplates at 2.6 × 10^4/well) for 2 h. The cells were washed twice using Dulbecco's Phosphate Buffered Saline (PBS, Euroclone) and 100 μl/well of fresh culture media were added. Following 72 h incubation, the Reed and Muench method was used to calculate the $TCID_{50}$/ml for each viral stock. The titer of HIV-1 virus stock was determined dosing the p24 antigen (HIV-1 capsid) by chemiluminescent immunoassay (ARCHITECT system, Abbott, USA).

4.6. Virus inhibition test

4.6.1. Method A

Cells were seeded in 96-well plates at a density of 1.3 × 10^4 cell/well and incubated for 24 h at 37 °C in 5% CO_2 and 95% humidity. They were then pre-treated with two-fold serial dilutions of the compounds starting from 80 μM (10μl/well) and the plates were incubated for another 24 h. Cell control wells were included. The non-adsorbed compounds were discarded, 100TCD_{50}/50 μl of viral stock for SARS-CoV-2, HSV-1 and Flu B or 400 fg of p24 antigen/50 μl of HIV-1 viral sock were added to the cells and incubated for 2 h at 37 °C. The infected cells were subsequently washed using PBS and treated with the compounds as described above. Virus control wells were included. Supernatants were collected 24 and 48 h post infection (hpi) for viral genome extraction.

4.6.2. Method B

Cells were seeded in 96-well plates at a density of 2.6 × 10^4 cell/well and incubated for 24 h at 37 °C in 5% CO_2 and 95% humidity. Two-fold serial dilutions of the compounds (starting from 80 μM) were mixed with 100TCD_{50}/well of virus stocks for 10 min. Cells were subsequently inoculated with SARS-CoV-2 virus/compound mixtures for 2 h at 37 °C. Following the above washing procedure, cells were incubated with the culture medium. Supernatants were collected 48 h post infection (hpi) for viral genome extraction.

4.6.3. Method C

Cells were seeded in 96-well plates at a density of 1.3 × 10^4 cell/well and incubated for 48 h at 37 °C in 5% CO_2 and 95% humidity. 100TCD_{50}/50 μl of SARS-CoV-2 viral stock were added to the cells and incubated for 2 h at 37 °C. The infected cells were subsequently washed using PBS and treated with the compounds as described above. Virus control wells were included. Supernatants were collected 24 and 48 h post infection (hpi)

4.7. Viral genome extraction and quantification by real-time PCR

Viral genome was extracted from supernatants using QIAsymphony DSP Virus/Pathogen Midi Kit according to manufacturer's instructions on the QIAsymphony automated platform (QIAGEN, Hilden, Germany) and quantified using Applied BiosystemsTM7500 Fast Dx Real-Time PCR Instrument (Thermo Fisher Scientific, Waltham, MA, USA). Real-time PCR assay of SARS-CoV-2 was performed using commercial set of

primers and probes (Integrated DNA Technologies, cat# 10006770) applying a protocol issued by the CDC (https://www.fda.gov/media/134922/download). Quantification of number of viral copies per milliliter of supernatant (cps/ml) was achieved using a calibration curve based on ten-fold serial dilutions (10^5 to 10^2 copies per reaction) of the WHO international standard for SARS- CoV-2 RNA (cat# 20/146), purchased from the National Institute for Biological Standards and Control (NIBSC). Calibration curve was included in each real-time session with a negative control. Real-Time PCR assay of HSV-1 was performed using oligonucleotide primers and probe (Forward primer: 5′-CGTCGGAGTTTTACCCAGAC-3'; reverse primer:5′-ACGCGATGAAGGCTTTC-3'; probe: FAM-AGTCAGGCCTGGTCGACTTTGTCACCBHQ1) designed to detect HSV-1 gene encoding DNA replication origin binding helicase in EXPRESS qPCR universal mix (Thermo Fisher Scientific, Waltham, MA, USA) according to manufacturer's instructions. Quantification of cps/ml of HSV-1 DNA per supernatant was achieved using a calibration curve based on ten-fold serial dilutions (10^5 to 10^2 copies per reaction) of standard plasmid containing specific gene. Calibration curve was included in each real-time session with negative control. Real-Time PCR assay of Flu B was performed using oligonucleotide primers and probe (Forward primer: 5′-TCCTCAAYTCACTCTTCGAGCG-3'; reverse primer:5′-CGGTGCTCTTGACCAAA TTGG-3'; probe: FAM-CCAATTCGAGCAGCTGAAACTGCGGTG-BHQ1) designed to detect Flu B gene encoding NS proteins in EXPRESS qPCR universal mix (Thermo Fisher Scientific, Waltham, MA, USA) according to manufacturer's instructions. The infectious virus particles of HIV-1 produced GFP-NEF fusion protein which made infected cells fluorescent after 24 h and fluorescent emission increased after 48 h. For this reason, the relative fluorescence values (RFV) were measured directly on the culture plate using the Fluoroskan Ascent (Thermo scientific) to evaluate the replicative capacity.

4.8. Molecular dynamics

The lipid raft has been modeled following the composition reported in the current literature. In detail, the outer leaflet is composed of phospholipids, saturated sphingolipids, and cholesterol, while the inner leaflet contains phospholipids and cholesterol [42]. Moreover, the 1-palmitoyl-2-oleoyl-*sn*-glycero-3-phosphocholine (POPC) (760.1 g/mol), palmitoyl-sphingomyelin (PSM) (703.03 g/mol), and cholesterol (Chol) (386,65 g/mol) are the most present lipid components, with a molar ratio of 2:1:1 respectively [68,69]. These conditions were then chosen to simulate the lipid raft efficiently. With the aim to respect the molar ratio, the outer raft leaflet has been modeled with 72 lipids, considering 16 POPC, 34 Chol, and 40 PSM molecules. The inner leaflet exhibited 73 lipids, comprising 61 POPC and 12 Chol molecules. The membrane model has been solvated with 6041 TIP3P water molecules and 15 Na+ and 15 Cl-ions have been included to reach the physiological condition of 0.15 M. The entire system has been generated using CHARMM-GUI [70] in a simulation box of 6.82 x 6.82 × 8.50 nm^3, and periodic boundary conditions (PBCs) have been used along all axes.

This model has been used to create 4 different systems: (i) lipid raft, (ii) lipid raft with GM1, (iii) lipid raft with GM1 and EGCG, and (iv) lipid raft with GM1 and EGCG-C18. One molecule of GM1 has been inserted in the lipid raft membrane, with a molar ratio of 1.76% respect to POPC, in line with the range of variable amounts of GM1 in lipid rafts [71]. EGCG and EGCG-C18 molecules have been added in the water phase, to better mimic the experimental conditions. In both cases, one molecule has been considered to better focus on the interactions with GM1. Systems (i) and (ii) have been modeled and simulated as controls to be sure about the reliability of the computational results since the lipid raft has a particularly complex structure and the presence of GM1 requires accurate treatment.

Each system underwent a minimization step followed by Molecular Dynamics simulations consisting of six cycles of equilibration, followed by a production phase of 200 ns using the NPT ensemble in semi-isotropic conditions.

For the evaluation of the direct interaction between EGCG-C18 and GM1, a TIP3P water box was built using CHARMM-GUI [70] of 10 x 10 × 10 nm^3, and periodic boundary conditions (PBCs) were used along all axes. The system after minimization underwent a full cycle of equilibration (10 ns) which was followed by a production phase of 200 ns using NVT (equilibration)/NPT (production) ensemble,

All the simulations have been performed using GROMACS 2023.3 version and CHARMM36 m force field [72]. Finally, the trajectories have been analyzed using Visual Molecular Dynamics (VMD) [73] and UCS Chimera software [74].

4.9. EGFR activation by flow cytometry

The level of the EGFR activation in Vero-E6 was evaluated by flow cytometry as previously described [57]. Cells were seeded in 6-well plates at a density of 2 × 10^5 cell/well and treated as previously described for the evaluation of the antiviral efficacy of drugs. Briefly, cells were pretreated with 5 μM EGCG-C18 for 24 h, followed by adding $100TCD_{50}$/50 μl of viral stock and incubating for 2 h at 37 °C. The infected cells were subsequently washed using PBS and treated with the compounds as described above. Simultaneously, the same experiment was carried out as a control without infecting the cells. Cells were collected by incubation with 0.25% trypsin-EDTA and then fixed for 20 min at room temperature using 2% paraformaldehyde. Before staining with antibodies targeting EGFR (Invitrogen, MA5-28104) and phospho-EGFR (Y1068) (R&D Systems, IC3570F), the cells were permeabilized for 30 min on ice in PBS containing 0.5% BSA and 0.025% Triton X-100. The anti-EGFR and anti-phospho-EGFR antibodies were incubated for 1 h in the dark at 4 °C. A minimum of 5000 cells per sample was analyzed under identical conditions. To inhibit potential phosphatase activity, sodium fluoride (NaF) and sodium orthovanadate (Na_3VO_4) were added to the staining and permeabilization buffers, each at a final concentration of 1 mM. Data analysis was performed using FCS Express 7 (De Novo Software). EGFR activation was quantified by calculating the percentage of EGFR phosphorylation, which was determined by dividing the geometric mean fluorescence intensity of phospho-EGFR by that of total EGFR.

4.10. Imaging and quantification of lipid raft by confocal microscopy and flow cytometry

Cellular lipid raft levels were estimated based on staining of GM1 with cholera toxin stain. Cells were pre-treated with selected compounds concentrations for 24 h, infected with SARS-CoV-2 for 2 h and then treated again with EGCG, and EGCG-C18 for additional 24 h. For the lipid raft imaging, cells were seeded on glass coverslips, washed with PBS and incubated with CTxB-fluorescein isothiocyanate (CTxB-FITC; 1.0 μg/mL; E_x/E_m = 495/525 nm; C1655, Sigma) in the DMEM medium for 30 min in the dark. Cells were washed three times with PBS, fixed for 10 min in 2% paraformaldehyde (PFA) and then counterstained with 1.0 μg/mL of 4′,6-diamidino-2-phenylindole (DAPI; E_x/E_m = 358/461 nm). The coverslips were mounted with ProLong Glass Antifade Mountant (P36984, Invitrogen) and visualized with Nikon A1R confocal laser scanning microscope. The images were acquired under 20x and 60x objectives by excitation with 405 and 488 wavelengths and finally processed using NIS-element software. For the quantification of GM1 expression, cells were seeded in 6-well plates, cultured overnight, and treated as previously described. Then, cells were collected by trypsinization, incubated with CTxB-FITC (1.0 μg/mL) in PBS for 30 min, fixed with 2% PFA for 10 min at rt and analyzed with Guava easyCyte flow cytometer (Merk-Millipore, MA, USA).

4.11. Fourier Transform InfraRed microspectroscopy (FTIRM)

FTIRM measurements were performed in duplicate at the ARI Lab of

Department of Life and Environmental Sciences, Università Politecnica delle Marche (Ancona, Italy). A Hyperion 3000 Vis-IR microscope coupled with a INVENIO-R interferometer and equipped with a HgCdTe (MCT_A) detector (Bruker Optics, Ettlingen, Germany) was used. Cells were deposited on IR transparent CaF_2 optical windows and let air-dry for 30 min. For each sample, ~50 microareas (30 × 30 μm^2) containing densely packed cell monolayers were selected by visible microscopy. On these areas, IR spectra were collected in transmission mode in the MIR region (4000–900 cm^{-1}), averaging 512 scans (spectral resolution 4 cm^{-1}, zero-filling factor 2, scanner velocity 40 kHz). A background spectrum was acquired on a clean CaF_2 window before each sample acquisition, with the same parameters used for cells' measurements. All the collected raw spectra were pre-processed by correction of the contribution of atmospheric carbon dioxide and water vapor and vector normalization, with the Atmospheric Compensation and the Vector Normalization routines of OPUS 7.5 software (Bruker Optics GmbH).

4.12. Incorporation of EGCG-C18 in lipid-rich areas by Raman MicroSpectroscopy (RMS)

A Horiba Jobin-Yvon XploRA Nano Raman Microspectrometer, equipped with a 785-nm diode laser was used as a source. All RMS measurements were acquired by using a 5 × objective (Olympus, Tokyo, Japan). The spectrometer was calibrated to the 520.7 cm^{-1} line of silicon prior to spectral acquisition. 1800 lines per mm grating were chosen. A 200 μm confocal pinhole was used for all measurements. The spectra were dispersed onto a 16-bit dynamic range Peltier cooled CCD detector. RMS measurements were performed on ~10 single cells for each experimental group, to assess the incorporation of EGCG-C18. Raman maps were acquired on squared/rectangular areas covering the entire cell of interest, collecting spectra with a step size of 2 μm. On each Raman map, the following values were calculated: the area of the band centered at 1660 cm^{-1}, representing the Amide I band of proteins, and the area of the band centered at 1450 cm^{-1}, representing the CH_2 groups, mainly of lipids.

4.13. ADME properties prediction

The ADMET properties of EGCG-C18 were predicted using the ADMET-AI web server (https://admet-ai.com) [75]. The platform employs pre-trained machine-learning models to estimate pharmacokinetic and toxicity-related endpoints. Canonical SMILES representations of the compounds were submitted to the web interface, and predictions were obtained for human intestinal absorption (HIA), blood–brain barrier (BBB) permeability, cytochrome P450 (CYP450) inhibition, AMES toxicity, and hepatotoxicity.

4.14. Statistical analysis

All data were presented as mean ± standard deviation. Statistical analyses were performed using GraphPad Prism (Version 8.4.2, Graphpad Software, San Diego, CA, USA). Nonlinear regression was performed to calculate 50% inhibitory concentration values (IC_{50}) using the inhibitor versus response. The statistical significance was determined by unpaired *t*-test with Welch's correction and was defined as $p < 0.05$.

CRediT authorship contribution statement

Cristina Minnelli: Writing – original draft, Visualization, Methodology, Investigation, Conceptualization. **Sara Caucci:** Visualization, Methodology, Investigation, Data curation. **Roberta Galeazzi:** Writing – original draft, Resources, Methodology, Investigation. **Emiliano Laudadio:** Visualization, Resources, Methodology, Investigation. **Elena Romagnoli:** Investigation. **Andrea Frontini:** Writing – original draft, Resources, Methodology. **Loredana Rao:** Investigation. **Valentina Notarstefano:** Visualization, Methodology, Investigation. **Tatiana Armeni:** Writing – review & editing, Supervision. **Brenda Romaldi:** Investigation, Data curation. **Stefano Menzo:** Writing – review & editing, Resources, Methodology, Conceptualization. **Giovanna Mobbili:** Writing – review & editing, Writing – original draft, Supervision, Methodology, Conceptualization.

Declaration of competing interest

The authors declare that they have no known competing financial interests or personal relationships that could have appeared to influence the work reported in this paper.

Appendix A. Supplementary data

Supplementary data to this article can be found online at https://doi.org/10.1016/j.cbi.2026.111971.

Data availability

No data was used for the research described in the article.

References

[1] D. Hawkes, J. Mak, Lipid membrane; a novel target for viral and bacterial pathogens, Curr. Drug Targets 7 (2006) 1615–1621, https://doi.org/10.2174/138945006779025455.
[2] A. Ono, E.O. Freed, Plasma membrane rafts play a critical role in HIV-1 assembly and release, Proc. Natl. Acad. Sci. U. S. A. 98 (2001) 13925–13930, https://doi.org/10.1073/pnas.241320298.
[3] T. Takahashi, T. Suzuki, Function of membrane rafts in viral lifecycles and host cellular response, Biochem Res Int 2011 (2011) 245090, https://doi.org/10.1155/2011/245090.
[4] L. Pelkmans, Secrets of caveolae- and lipid raft-mediated endocytosis revealed by mammalian viruses, Biochim. Biophys. Acta Mol. Cell Res. 1746 (2005) 295–304, https://doi.org/10.1016/j.bbamcr.2005.06.009.
[5] Q. Wang, Y. Zhang, L. Wu, S. Niu, C. Song, Z. Zhang, G. Lu, C. Qiao, Y. Hu, K. Y. Yuen, Q. Wang, H. Zhou, J. Yan, J. Qi, Structural and functional basis of SARS-CoV-2 entry by using human ACE2, Cell 181 (2020) 894–904, https://doi.org/10.1016/j.cell.2020.03.045.
[6] R. Yan, Y. Zhang, Y. Li, L. Xia, Y. Guo, Q. Zhou, Structural basis for the recognition of SARS-CoV-2 by full-length human ACE2, Science 367 (2020) 1444–1448, https://doi.org/10.1126/science.abb2762.
[7] J. Fantini, H. Chahinian, N. Yahi, Convergent evolution dynamics of SARS-CoV-2 and HIV surface envelope glycoproteins driven by host cell surface receptors and lipid rafts: lessons for the future, Int. J. Mol. Sci. 24 (2023) 1923, https://doi.org/10.3390/IJMS24031923.
[8] W. Popik, T.M. Alce, W.-C. Au, Human immunodeficiency virus type 1 uses lipid raft-colocalized CD4 and chemokine receptors for productive entry into CD4 + T cells, J. Virol. 76 (2002) 4709–4722, https://doi.org/10.1128/jvi.76.10.4709-4722.2002.
[9] D.H. Nguyen, D. Taub, CXCR4 function requires membrane cholesterol: implications for HIV infection, J. Immunol. 168 (2002) 4121–4126, https://doi.org/10.4049/jimmunol.168.8.4121.
[10] M. Viard, I. Parolini, M. Sargiacomo, K. Fecchi, C. Ramoni, S. Ablan, F.W. Ruscetti, J.M. Wang, R. Blumenthal, Role of cholesterol in human immunodeficiency virus type 1 envelope protein-mediated fusion with host cells, J. Virol. 76 (2002) 11584–11595, https://doi.org/10.1128/jvi.76.22.11584-11595.2002.
[11] H. Huang, Y. Li, T. Sadaoka, H. Tang, T. Yamamoto, K. Yamanishi, Y. Mori, Human herpesvirus 6 envelope cholesterol is required for virus entry, J. Gen. Virol. 87 (2006) 277–285, https://doi.org/10.1099/vir.0.81551-0.
[12] H. Tang, A. Kawabata, M. Takemoto, K. Yamanishi, Y. Mori, Human herpesvirus-6 infection induces the reorganization of membrane microdomains in target cells, which are required for virus entry, Virology 378 (2008) 265–271, https://doi.org/10.1016/j.virol.2008.05.028.
[13] A. Kawabata, H. Tang, H. Huang, K. Yamanishi, Y. Mori, Human herpesvirus 6 envelope components enriched in lipid rafts: evidence for virion-associated lipid rafts, Virol. J. 6 (2009) 127, https://doi.org/10.1186/1743-422X-6-127.
[14] F. Santoro, P.E. Kennedy, G. Locatelli, M.S. Malnati, E.A. Berger, P. Lusso, CD46 is a cellular receptor for human herpesvirus 6, Cell 99 (1999) 817–827, https://doi.org/10.1016/s0092-8674(00)81678-5.
[15] T. Das, C. Mukhopadhyay, Identification of possible binding modes of SARS-CoV-2 spike N-terminal domain for ganglioside GM1, Chem. Phys. Lett. 812 (2023) 140260, https://doi.org/10.1016/j.cplett.2022.140260.
[16] T. Das, C. Mukhopadhyay, Comparison and possible binding orientations of SARS-CoV-2 spike N-Terminal domain for gangliosides GM3 and GM1, J. Phys. Chem. B 127 (2023) 6940–6948, https://doi.org/10.1021/ACS.JPCB.3C02286.
[17] M. Matveeva, M. Lefebvre, H. Chahinian, N. Yahi, J. Fantini, Host membranes as drivers of virus evolution, Viruses 15 (2023) 1854, https://doi.org/10.3390/V15091854.

[18] M. Lefebvre, H. Chahinian, B. La Scola, J. Fantini, Characterization and fluctuations of an ivermectin binding site at the lipid raft interface of the N-Terminal domain (NTD) of the spike protein of SARS-CoV-2 variants, Viruses 16 (2024) 1836, https://doi.org/10.3390/V16121836.

[19] D. Sviridov, Y.I. Miller, R.A. Ballout, A.T. Remaley, M. Bukrinsky, Targeting lipid Rafts—A potential therapy for COVID-19, Front. Immunol. 11 (2020) 574508, https://doi.org/10.3389/fimmu.2020.574508.

[20] S.N. Palacios-Rápalo, L.A. De Jesús-González, C.D. Cordero-Rivera, C.N. Farfan-Morales, J.F. Osuna-Ramos, G. Martínez-Mier, J. Quistián-Galván, A. Muñoz-Pérez, V. Bernal-Dolores, R.M. del Ángel, J.M. Reyes-Ruiz, Cholesterol-Rich lipid rafts as platforms for SARS-CoV-2 entry, Front. Immunol. 12 (2021) 796855, https://doi.org/10.3389/fimmu.2021.796855.

[21] R. Roncato, J. Angelini, A. Pani, R. Talotta, Lipid rafts as viral entry routes and immune platforms: a double-edged sword in SARS-CoV-2 infection? Biochim. Biophys. Acta Mol. Cell Biol. Lipids 1867 (2022) 159140 https://doi.org/10.1016/j.bbalip.2022.159140.

[22] X. Li, W. Zhu, M. Fan, J. Zhang, Y. Peng, F. Huang, N. Wang, L. He, L. Zhang, R. Holmdahl, L. Meng, S. Lu, Dependence of SARS-CoV-2 infection on cholesterol-rich lipid raft and endosomal acidification, Comput. Struct. Biotechnol. J. 19 (2021) 1933–1943, https://doi.org/10.1016/J.CSBJ.2021.04.001.

[23] Y. Lu, D.X. Liu, J.P. Tam, Lipid rafts are involved in SARS-CoV entry into Vero E6 cells, Biochem. Biophys. Res. Commun. 369 (2008) 344–349, https://doi.org/10.1016/j.bbrc.2008.02.023.

[24] M. El Khoury, H.Y. Naim, Lipid rafts disruption by statins negatively impacts the interaction between SARS-CoV-2 S1 subunit and ACE2 in intestinal epithelial cells, Front. Microbiol. 14 (2024) 1335458, https://doi.org/10.3389/fmicb.2023.1335458.

[25] A.M. Gorabi, N. Kiaie, V. Bianconi, T. Jamialahmadi, K. Al-Rasadi, T.P. Johnston, M. Pirro, A. Sahebkar, Antiviral effects of statins, Prog. Lipid Res. 79 (2024) 101054, https://doi.org/10.1016/j.plipres.2020.101054.

[26] C. Bailly, G. Vergoten, Glycyrrhizin: an alternative drug for the treatment of COVID-19 infection and the associated respiratory syndrome? Pharmacol. Ther. 214 (2020) 107618 https://doi.org/10.1016/j.pharmthera.2020.107618.

[27] T. Ohishi, T. Hishiki, M.S. Baig, S. Rajpoot, U. Saqib, T. Takasaki, Y. Hara, Epigallocatechin gallate (EGCG) attenuates severe acute respiratory coronavirus disease 2 (SARS-CoV-2) infection by blocking the interaction of SARS-CoV-2 spike protein receptor-binding domain to human angiotensin-converting enzyme 2, PLoS One 17 (2022) e0271112, https://doi.org/10.1371/journal.pone.0271112.

[28] Y. Fujimura, H. Tachibana, K. Yamada, Lipid raft-associated catechin suppresses the FcεRI expression by inhibiting phosphorylation of the extracellular signal-regulated kinase1/2, FEBS Lett. 556 (2004) 204–210, https://doi.org/10.1016/S0014-5793(03)01432-7.

[29] S.K. Patra, F. Rizzi, A. Silva, D.O. Rugina, S. Bettuzzi, Molecular targets of (-)-epigallocatechin-3-gallate (EGCG): specificity and interaction with membrane lipid rafts, J. Physiol. Pharmacol. 59 (2008) 19261982. https://pubmed.ncbi.nlm.nih.gov/19261982/.

[30] J. Liu, B.H. Bodnar, F. Meng, A.I. Khan, X. Wang, S. Saribas, T. Wang, S.C. Lohani, P. Wang, Z. Wei, J. Luo, L. Zhou, J. Wu, G. Luo, Q. Li, W. Hu, W. Ho, Epigallocatechin gallate from green tea effectively blocks infection of SARS-CoV-2 and new variants by inhibiting spike binding to ACE2 receptor, Cell Biosci. 11 (2021) 1–15, https://doi.org/10.1186/s13578-021-00680-8.

[31] V. Tsvetkov, A. Varizhuk, L. Kozlovskaya, A. Shtro, O. Lebedeva, A. Komissarov, T. Vedekhina, V. Manuvera, O. Zubkova, A. Eremeev, E. Shustova, G. Pozmogova, D. Lioznov, A. Ismukhametov, V. Lazarev, M. Lagarkova, EGCG as an anti-SARS-CoV-2 agent: preventive versus therapeutic potential against original and mutant virus, Biochimie 191 (2021) 27–32, https://doi.org/10.1016/j.biochi.2021.08.003.

[32] S. Adachi, T. Nagao, H.I. Ingolfsson, F.R. Maxfield, O.S. Andersen, L. Kopelovich, I. B. Weinstein, The inhibitory effect of (−)-Epigallocatechin gallate on activation of the epidermal growth factor receptor is associated with altered lipid order in HT29 Colon cancer cells, Cancer Res. 67 (2007) 6493–6501, https://doi.org/10.1158/0008-5472.can-07-0411.

[33] M. Hao, S. Mukherjee, Y. Sun, F.R. Maxfield, Effects of cholesterol depletion and increased lipid unsaturation on the properties of endocytic membranes, J. Biol. Chem. 279 (2004) 14171–14178, https://doi.org/10.1074/jbc.m309793200.

[34] C. Minnelli, R. Galeazzi, E. Laudadio, A. Amici, D. Rusciano, T. Armeni, M. Cantarini, P. Stipa, G. Mobbili, Monoalkylated epigallocatechin-3-gallate (C18-EGCG) as novel lipophilic EGCG derivative: characterization and antioxidant evaluation, Antioxidants 9 (2020) 208, https://doi.org/10.3390/antiox9030208.

[35] S. Singh, P. Ghosh, R. Roy, A. Behera, R. Sahadevan, P. Kar, S. Sadhukhan, A. Sonawane, 4″-Alkyl EGCG derivatives induce cytoprotective autophagy response by inhibiting EGFR in glioblastoma cells, ACS Omega 9 (2024) 2286–2301, https://doi.org/10.1021/ACSOMEGA.3C06110.

[36] C. Minnelli, E. Laudadio, R. Galeazzi, D. Rusciano, T. Armeni, P. Stipa, M. Cantarini, G. Mobbili, Synthesis, characterization and antioxidant properties of a new lipophilic derivative of edaravone, Antioxidants 8 (2020) 258, https://doi.org/10.3390/antiox8080258.

[37] H. Byrne, G. Sockalingum, N. Stone, Raman spectroscopy: complement or competitor?, in: D. Moss (Ed.), Biomedical Applications of Synchrotron Infrared Microspectroscopy Royal Society of Chemistry, RCS Analytical Spectroscopy Monographs, 2011, pp. 105–142, 11.

[38] V. Notarstefano, G. Gioacchini, H.J. Byrne, C. Zacà, E. Sereni, L. Vaccari, A. Borini, O. Carnevali, E. Giorgini, Vibrational characterization of granulosa cells from patients affected by unilateral ovarian endometriosis: new insights from infrared and raman microspectroscopy, Spectrochim. Acta Mol. Biomol. Spectrosc. 212 (2019) 206–214, https://doi.org/10.1016/j.saa.2018.12.054.

[39] V. Notarstefano, M. Pisani, M. Bramucci, L. Quassinti, F. Maggi, L. Vaccari, M. Parlapiano, E. Giorgini, P. Astolfi, A vibrational in vitro approach to evaluate the potential of monoolein nanoparticles as isofuranodiene carrier in MDA-MB 231 breast cancer cell line: new insights from infrared and raman microspectroscopies, Spectrochim. Acta Mol. Biomol. Spectrosc. 269 (2022) 120735–120747, https://doi.org/10.1016/j.saa.2021.120735.

[40] M. Trybus, A. Hryniewicz-Jankowska, K. Wójtowicz, T. Trombik, A. Czogalla, A. F. Sikorski, EFR3A: a new raft domain organizing protein? Cell. Mol. Biol. Lett. 28 (2023) 86, https://doi.org/10.1186/S11658-023-00497-Y.

[41] D.A. Brown, Preparation of detergent-resistant membranes (DRMs) from cultured mammalian cells, Methods Mol. Biol. 1232 (2015) 55–64, https://doi.org/10.1007/978-1-4939-1752-5_5.

[42] K. Simons, R. Ehehalt, Cholesterol, lipid rafts, and disease, J. Clin. Investig. 110 (2002) 597–603, https://doi.org/10.1172/JCI16390.

[43] M. Sorice, R. Misasi, G. Riitano, V. Manganelli, S. Martellucci, A. Longo, T. Garofalo, V. Mattei, Targeting lipid rafts as a strategy against coronavirus, Front. Cell Dev. Biol. 8 (2021) 618296, https://doi.org/10.3389/fcell.2020.618296.

[44] C. McQuaid, A. Solorzano, I. Dickerson, R. Deane, Uptake of severe acute respiratory syndrome coronavirus 2 spike protein mediated by angiotensin converting enzyme 2 and ganglioside in human cerebrovascular cells, Front. Neurosci. 17 (2023) 1116845, https://doi.org/10.3389/fnins.2023.1117845.

[45] J. Fantini, H. Chahinian, N. Yahi, Synergistic antiviral effect of hydroxychloroquine and azithromycin in combination against SARS-CoV-2: what molecular dynamics studies of virus-host interactions reveal, Int. J. Antimicrob. Agents 56 (2020) 106020, https://doi.org/10.1016/j.ijantimicag.2020.106020.

[46] E.S. Heinl, S. Lorenz, B. Schmidt, N. Nasser M Laqtom, J.R. Mazzulli, L. Francelle, T.W. Yu, B. Greenberg, S. Storch, I. Tegtmeier, H. Othmen, K. Maurer, M. Steinfurth, R. Witzgall, V. Milenkovic, C.H. Wetzel, M. Reichold, CLN7/MFSD8 may be an important factor for SARS-CoV-2 cell entry, iScience 25 (2022) 105082, https://doi.org/10.1016/J.ISCI.2022.105082.

[47] T. Gianni, G. Campadelli-Fiume, αVβ3-integrin relocalizes nectin1 and routes herpes simplex virus to lipid rafts, J. Virol. 86 (2012) 2850–2855, https://doi.org/10.1128/JVI.06689-11.

[48] A.J. Iacano, H. Lewis, J.E. Hazen, H. Andro, J.D. Smith, K. Gulshan, Miltefosine increases macrophage cholesterol release and inhibits NLRP3-inflammasome assembly and IL-1β release, Sci. Rep. 9 (2019) 11128, https://doi.org/10.1038/s41598-019-47610-w.

[49] A. Somogyi, A. Petcherski, B. Beckert, M. Huebecker, D.A. Priestman, A. Banning, S.L. Cotman, F.M. Platt, M.O. Ruonala, R. Tikkanen, Altered expression of ganglioside metabolizing enzymes results in GM3 ganglioside accumulation in cerebellar cells of a mouse model of juvenile neuronal ceroid lipofuscinosis, Int. J. Mol. Sci. 19 (2018) 625, https://doi.org/10.3390/IJMS19020625.

[50] D. Lingwood, B. Binnington, T. Róg, I. Vattulainen, M. Grzybek, Ü. Coskun, C. A. Lingwood, K. Simons, Cholesterol modulates glycolipid conformation and receptor activity, Nat. Chem. Biol. 7 (2011) 260–262, https://doi.org/10.1038/nchembio.551.

[51] E. Sezgin, I. Levental, M. Grzybek, G. Schwarzmann, V. Mueller, A. Honigmann, V. N. Belov, C. Eggeling, Ü. Coskun, K. Simons, P. Schwille, Partitioning, diffusion, and ligand binding of raft lipid analogs in model and cellular plasma membranes, Biochim. Biophys. Acta Biomembr. 1818 (2012) 1777–1784, https://doi.org/10.1016/J.BBAMEM.2012.03.007.

[52] E. Laudadio, L. Mangano, C. Minnelli, Chemical scaffolds for the clinical development of mutant-selective and reversible fourth-generation EGFR-TKIs in NSCLC, ACS Chem. Biol. 19 (2024) 839–854, https://doi.org/10.1021/acschembio.4c00028.

[53] A. Razzaq, C. Disoma, Y. Zhou, S. Tao, Z. Chen, S. Liu, R. Zheng, Y. Zhang, Y. Liao, X. Chen, S. Liu, Z. Dong, L. Xu, X. Deng, S. Li, Z. Xia, Targeting epidermal growth factor receptor signalling pathway: a promising therapeutic option for COVID-19, Rev. Med. Virol. 34 (2024) e2500, https://doi.org/10.1002/rmv.2500.

[54] A.R. Palakkott, A. Alneyadi, K. Muhammad, A.H. Eid, K.M.A. Amiri, M. Akli Ayoub, R. Iratni, The SARS-CoV-2 spike protein activates the epidermal growth factor receptor-mediated signaling, Vaccines (Basel) 11 (2023) 768, https://doi.org/10.3390/vaccines11040768.

[55] C.Z. Chen, M. Xu, M. Pradhan, K. Gorshkov, J.D. Petersen, M.R. Straus, W. Zhu, P. Shinn, H. Guo, M. Shen, C. Klumpp-Thomas, S.G. Michael, J. Zimmerberg, W. Zheng, G.R. Whittaker, Identifying SARS-CoV-2 entry inhibitors through drug repurposing screens of SARS-S and MERS-S pseudotyped particles, ACS Pharmacol. Transl. Sci. 3 (2020) 1165–1175, https://doi.org/10.1021/acsptsci.0c00112.

[56] A. Schreiber, D. Viemann, J. Schöning, S. Schloer, A. Mecate Zambrano, L. Brunotte, A. Faist, M. Schöfbänker, E. Hrincius, H. Hoffmann, M. Hoffmann, S. Pöhlmann, U. Rescher, O. Planz, S. Ludwig, The MEK1/2-inhibitor ATR-002 efficiently blocks SARS-CoV-2 propagation and alleviates pro-inflammatory cytokine/chemokine responses, Cell. Mol. Life Sci. 79 (2022) 65, https://doi.org/10.1007/S00018-021-04085-1.

[57] C. Minnelli, L. Cianfruglia, E. Laudadio, M. Giovanna, R. Galeazzi, T. Armeni, Effect of epigallocatechin-3-gallate on egfr signaling and migration in non-small cell lung cancer, Int. J. Mol. Sci. 22 (2021) 11833, https://doi.org/10.3390/ijms222111833.

[58] C. Minnelli, E. Laudadio, G. Mobbili, R. Galeazzi, Conformational insight on WT- and Mutated-EGFR receptor activation and inhibition by Epigallocatechin-3-Gallate: over a rational basis for the design of selective non-small-cell lung anticancer agents, Int. J. Mol. Sci. 21 (2021) 1721, https://doi.org/10.3390/ijms21051721.

[59] Ü. Coskun, M. Grzybek, D. Drechsel, K. Simons, Regulation of human EGF receptor by lipids, Proc. Natl Acad Sci U. S. A. 108 (2011) 9044–9904, https://doi.org/10.1073/pnas.1105666108.

[60] E. Sean, Computational Toxicology: Risk Assessment for Chemicals, John Wiley & Sons, Hoboken, NJ, 2018.
[61] C.A. Lipinski, F. Lombardo, B.W. Dominy, P.J. Feeney, Experimental and computational approaches to estimate solubility and permeability in drug discovery and development settings, Adv. Drug Deliv. Rev. 46 (2001) 3–26, https://doi.org/10.1016/S0169-409X(00)00129-0.
[62] U.M. Zanger, M. Schwab, Cytochrome P450 enzymes in drug metabolism: regulation of gene expression, enzyme activities, and impact of genetic variation, Pharmacol. Ther. 138 (2013) 103–141, https://doi.org/10.1016/j.pharmthera.2012.12.007.
[63] M.C. Sanguinetti, M. Tristani-Firouzi, hERG potassium channels and cardiac arrhythmia, Nature 440 (2006) 463–469, https://doi.org/10.1038/NATURE04710.
[64] S. Singh, R. Sahadevan, R. Roy, M. Biswas, P. Ghosh, P. Kar, A. Sonawane, S. Sadhukhan, Structure-based design and synthesis of a novel long-chain 4″-alkyl ether derivative of EGCG as potent EGFR inhibitor: in vitro and in silico studies, RSC Adv. 12 (2022) 17821–17836, https://doi.org/10.1039/D2RA01919A.
[65] G. Mobbili, B. Romaldi, G. Sabbatini, A. Amici, M. Marcaccio, R. Galeazzi, E. Laudadio, T. Armeni, C. Minnelli, Identification of flavone derivative displaying a 4′-Aminophenoxy moiety as potential selective anticancer agent in NSCLC tumor cells, Molecules 28 (2023), https://doi.org/10.3390/molecules28073239.
[66] F. Alessandrini, S. Caucci, V. Onofri, F. Melchionda, A. Tagliabracci, P. Bagnarelli, L. Di Sante, C. Turchi, S. Menzo, Evaluation of the ion AmpliSeq SARS-CoV-2 research panel by massive parallel sequencing, Genes 11 (2020) 1–14, https://doi.org/10.3390/GENES11080929.
[67] S. Menzo, S. Rusconi, A. Monachetti, M.C. Colombo, M. Violin, P. Bagnarelli, P. E. Varaldo, M. Moroni, M. Galli, C. Balotta, M. Clementi, Quantitative evaluation of the recombinant HIV-1 phenotype to protease inhibitors by a single-step strategy, AIDS 14 (2000) 1101–1110, https://doi.org/10.1097/00002030-200006160-00006.
[68] Y. Nagatsuka, Y. Hirabayashi, Phosphatidylglucoside: a new marker for lipid rafts, Biochim. Biophys. Acta 1780 (2008) 405–409, https://doi.org/10.1016/j.bbagen.2007.08.016.
[69] P.S. Niemelä, M.T. Hyvönen, I. Vattulainen, Atom-scale molecular interactions in lipid raft mixtures, Biochim. Biophys. Acta Biomembr. 1788 (2009) 122–135, https://doi.org/10.1016/j.bbamem.2008.08.018.
[70] S. Jo, T. Kim, V.G. Iyer, W. Im, CHARMM-GUI: a web-based graphical user interface for CHARMM, J. Comput. Chem. 29 (2008) 1859–1865, https://doi.org/10.1002/jcc.20945.
[71] K.V. Pavlov, S.A. Akimov, P.V. Bashkirov, I.A. Boldyrev, W.G. Tellford, I. M. Molotkovskaya, Influence of ganglioside GM1 on formation and properties of rafts in lipid membranes, Biophys. J. 96 (2009) 448a, https://doi.org/10.1016/j.bpj.2008.12.2305.
[72] J. Huang, A.D. Mackerell, CHARMM36 all-atom additive protein force field: validation based on comparison to NMR data, J. Comput. Chem. 34 (2013) 2135–2145, https://doi.org/10.1002/jcc.23354.
[73] W. Humphrey, A. Dalke, K. Schulten, VMD: visual molecular dynamics, J. Mol. Graph. 14 (1996) 33–38, https://doi.org/10.1016/0263-7855(96)00018-5.
[74] E.F. Pettersen, T.D. Goddard, C.C. Huang, G.S. Couch, D.M. Greenblatt, E.C. Meng, T.E. Ferrin, UCSF chimera—A visualization system for exploratory research and analysis, J. Comput. Chem. 25 (2004) 1605–1612, https://doi.org/10.1002/jcc.20084.
[75] K. Swanson, P. Walther, J. Leitz, S. Mukherjee, J.C. Wu, R.V. Shivnaraine, J. Zou, ADMET-AI: a Machine Learning ADMET Platform for Evaluation of large-scale Chemical Libraries, BioRxiv, 2023 573531, https://doi.org/10.1101/2023.12.28.573531.